

## Article

# Thermal-Hydraulic-Mechanical (THM) Modelling of Short-Term Gas Storage in a Depleted Gas Reservoir—A Case Study from South Germany <sup>†</sup>

Muhammad Zain-Ul-Abedin \*  and Andreas Henk \* 

Institute of Applied Geosciences, Technical University of Darmstadt, 64287 Darmstadt, Germany

\* Correspondence: abedin@geo.tu-darmstadt.de (M.Z.-U.A.); henk@geo.tu-darmstadt.de (A.H.);

Tel.: +49-6151-1622-347 (M.Z.-U.A.); +49-6151-1622-344 (A.H.)

<sup>†</sup> This paper is an extended version of my PhD thesis with title “Coupled Thermal-Hydraulic-Mechanical (THM) Modelling of Underground Gas Storage—A Case from the Molasse Basin, South Germany” submitted in 2022 Technical university of Darmstadt, Darmstadt, Germany, March 2022; p. 103.

**Abstract:** This study addresses the use of former gas storage facilities as short-term storage for renewable energy through power-to-gas (PtG) technology in Germany. Three test cases with coupled thermal-hydronechanical (THM) modelling were conducted to evaluate short-term injection and production schedules. The operating rates were controlled by the upper and lower limits of the wellbore pressure. The maximum difference in pore pressure and effective stress was 0.6 MPa in all cases. Fault reactivation analysis was performed on the THM models to estimate fault stability. The critical pore pressure for safe reservoir operation was determined to be 1.25 times the original pore pressure, corresponding to a WBHP value of 20.25 MPa. The upper limit of the gas injection rate for safe storage operation was estimated to be between 100,000 and 150,000 m<sup>3</sup>/day. The thermal stresses were found to be negligible for short-term cases. The storage capacity of PtG technology was reported to be up to 1,322,400 kWh/d of renewable electricity, which can contribute to Germany becoming a greenhouse gas neutral country by 2050. The workflows and results of the study are applicable to all gas storage in a porous medium, including methane, CO<sub>2</sub>, and hydrogen.

**Keywords:** THM modelling; short term underground gas storage; dynamic modelling; “battery” for power-to-gas



**Citation:** Zain-Ul-Abedin, M.; Henk, A. Thermal-Hydraulic-Mechanical (THM) Modelling of Short-Term Gas Storage in a Depleted Gas Reservoir—A Case Study from South Germany. *Energies* **2023**, *16*, 3389. <https://doi.org/10.3390/en16083389>

Academic Editors:

Luis Hernández-Callejo,  
Jesús Armando Aguilar Jiménez  
and Carlos Meza Benavides

Received: 27 February 2023

Revised: 5 April 2023

Accepted: 10 April 2023

Published: 12 April 2023



**Copyright:** © 2023 by the authors. Licensee MDPI, Basel, Switzerland. This article is an open access article distributed under the terms and conditions of the Creative Commons Attribution (CC BY) license (<https://creativecommons.org/licenses/by/4.0/>).

## 1. Introduction

High energy demand has intensified research into the “underground gas storage” (UGS) discipline [1]. As a result, both long-term (seasonal) and short-term (weekly) gas storage projects have gained the attention of UGS researchers [1]. An idea in this context is to store methane produced by “power-to-gas (PtG)” technology from excessive electricity produced by renewable sources, such as solar and wind. The stored gas can then be reused for power generation whenever needed. Thus, UGS is used as a kind of “battery” for surplus green energy.

Short-term storage cycles may cause some geomechanical issues in the porous reservoir. The pore fluid pressure in the reservoir fluctuates due to intensive gas injection and withdrawal phases. These fluctuations in fluid pressure change the effective stresses in the reservoir and may also change the in-situ stress state outside the reservoir area [2]. These changes have implications for geomechanical phenomena related to fault stability, caprock integrity, and surface deformation. Numerical modelling, e.g., 3D geomechanical modelling, provides a platform to integrate lithological and mechanical heterogeneities and investigate stress state changes during injection-production cycles of high frequency.

This study concentrates on a geomechanical assessment of a former gas field in the Bavarian Molasse Basin east of Munich (Germany) for which a hypothetical transformation into an UGS site is investigated. Various scenarios with variable short-term (weekly)

schedules to test cases for gas storage and withdrawal are considered to evaluate stresses (e.g., effective stress) and deformation due to pressure changes with high-frequency injection/production cycles. German data for excess electricity from renewable energy sources (such as solar and wind) throughout the calendar year 2017 are also considered in two cases to address the issue of irregular schedules in gas supply (via PtG) and energy demand.

The modelling results provide information about the stress state within and around the reservoir because of the production and injection of each selected time step, and they are compared with the stress states at the depletion and replenishment stages. The production history of the reservoir (porous media) is categorically useful to determine stress paths within and around the reservoir and wellbore periphery, as well as caprock integrity. Further, the modelling results provide information about ground surface subsidence during peak depletion and replenishment time steps, which can be useful to minimize geomechanical risks to any gas storage facility, not only for methane or CO<sub>2</sub> but also for hydrogen. Finally, fault reactivation analyses are also incorporated to obtain a safe gas injection rate for safe storage capacity.

The most popular gas storage method is underground gas storage among others, such as liquefied natural gas (LNG), storage tanks, and pipeline storage [3,4]. Two important issues are associated with UGS. First, it relies on gas imports due to increased demand for power generation (gas-to-power) and other domestic usages. Second, any damage to infrastructure could lead to higher gas prices or disruption of supply, with unpredictable, costly consequences for customers [1]. To address these challenges, various research has suggested using depleted gas/oil porous reservoirs or aquifers as UGS, with which significant volumes can be strategically stored [1,5].

One of the main advantages of depleted gas reservoirs is that they allow convenient and cost-effective gas storage, as they have suitable permeability properties and pore connections [6,7]. Some vital data, such as geological and geophysical characteristics, petrophysical properties, storage capacity, pressure, and the production history of depleted gas reservoirs, have been thoroughly studied and well recorded during the development phase of the reservoir field, enabling numerical modelling to simulate the injection-production process of underground gas reservoirs [3,6,8].

Water encroachment occurs in the porous reservoir vertically and laterally during the development phase of the gas reservoir. This water invasion causes fewer porous spaces in the reservoir, and different fluid distribution areas are formed in the longitudinal and traverse planes of the reservoir. During the injection and production operations of gas storage, the gas-water interface moves downward when gas is injected and moves upward when gas is produced [9]. Furthermore, as the foreign gas is injected into the reservoir, which has a different temperature than the reservoir's actual temperature, these thermal changes in the reservoir also cause some thermal stress changes in the reservoir, which is not the case in the reservoir exploitation phase. Therefore, it is necessary to conduct a systematic modelling study of the changes in the thermal-hydraulic-mechanical properties of UGS due to repeated water intrusion and multiphase seepage rules during high-speed injection production operations. The state-of-the-art thermal-hydro-mechanical (THM) modelling provides a platform to analyse and investigate all these issues related to porous UGS systems discussed above. THM models are typically derived from a wide range of geological, geophysical, and engineering data, including field measurements, core tests, well logs, drilling, and production data. After calibration, these THM models can be used for ground surface subsidence, thermal stress changes, maximum safe storage capacity, and maximum threshold pressure, avoiding fault reactivation and maintaining caprock integrity [10–12].

This modelling case study is a THM assessment of a former depleted gas reservoir field from the Molasse Basin in South Germany and has been presented in [10]. This dynamic modelling study addresses the following issues related to short-term and long-term operations of UGS: (1) the storage capacity of the reservoir; (2) thermal analysis with changing temperatures of the reservoir due to the injection of gas; (3) potential fault

reactivation analysis; and (4) stress path changes due to changes in pore pressure because of short-term production/injection cycles. These types of THM models, particularly short-term scheduled models, have implications for PtG technology in which simulations help us to understand that excess power from renewable resources can be stored in underground gas storage reservoirs and vice versa.

## 2. Methodology

### 2.1. Hydraulic Model

The flow simulation accounts for multiphase fluid flow in porous media. A hydraulic model is usually conducted by reservoir simulation, i.e., a form of numerical modelling in which physical phenomena are quantified and interpreted throughout the history of a reservoir and beyond, with the ability to extend this model to future performances. Reservoir simulation is a proven and effective method for dealing with uncertainties during exploration and production [13]. It is also helpful to determine the amount of gas that can be stored in each underground gas (CO<sub>2</sub>, hydrogen, or methane) storage reservoir [13]. The physical phenomenon behind (fluid flow) reservoir simulations are based mainly Darcy's law and mass material balance [10].

The composition of the fluid can be treated in different ways in reservoir simulations. Black oil simulators assume oil and gas phases to be one component through space and time. The properties of this component can change with pressure and temperature, while the composition does not change [13]. Thereby, the behaviour of the multiphase system can be described by complex PVT (pressure, volume, temperature) and SCAL (special core analysis) relations [13].

As a general solution method, the reservoir is divided into several cells with provided petrophysical properties, such as porosity and permeability. Then, the wells are placed within cells, and production rates are provided with different time steps. Last, the equations are solved to determine the pressure, temperature, and saturation for each cell. Each cell is solved simultaneously; therefore, the number of cells in the reservoir simulation is directly related to the time required to solve a time step [13].

### 2.2. Thermal Model

The thermal-flow-stress simulation model considers the proportional heat transfer in porous media when considering the multi-fluid flow concept in a THM simulation. The thermal flow model is usually performed by numerical modelling, in which the thermal hydraulic aspects are quantified together with the geomechanical simulation and interpreted throughout the history of a reservoir and storage operations in underground gas storage facilities. The main governing law in the thermal modelling is Fourier's law, also known as the law of heat conduction. The law states that the rate of heat transfer through a material is proportional to the negative temperature gradient and to the area at right angles to that gradient through which the heat flows. The governing equation of Fourier's law describes that the local heat flux density ( $q_h$ ) is equal to the product of the thermal conductivity ( $k_t$ ) and the negative local temperature gradient ( $-\nabla T$ ) [14]:

$$q_h = -k_t \nabla T, \quad (1)$$

where  $q_h$  is in (W/m<sup>2</sup>),  $k_t$  is in (W/m·K), and  $\nabla T$  is in (K/m). Fourier's law can also be used in uni-dimensional form in any direction,  $i, j, k$ ; for that reason, the equation becomes:

$$q_h = -k_t \frac{dT}{d(i, j, k)}, \quad (2)$$

### 2.3. Coupled Thermal-Hydraulic-Mechanical (THM) Modelling

The coupling of a reservoir simulator with a geomechanics module is an integral component for analysing hydrocarbon reservoirs in petroleum, underground gas storage, and the geothermal industry. A conventional geomechanical simulator provides surface

subsidence, which is often estimated using a simple mechanical formula without knowing the full geomechanical response. The only geomechanical parameter considered may be the pore compressibility, which is not sufficient to reproduce the changes in pore volume caused by complex pressure and temperature variations [15,16]. For some problems, such as primary production and linear elastic responses of reservoirs, subsidence calculated by a reservoir simulator alone can produce results comparable to coupled solutions [16,17].

In a coupled simulator, flow can be strongly influenced by the stress and strain distributions that lead to changes in porosity and permeability, but effective stress changes are ignored in conventional simulation methods. Such approaches cannot provide adequate predictions when considering a stress-sensitive reservoir (e.g., underground gas storage reservoir) [15,18]. There are two main components of coupling: volume coupling and fluid flow coupling according to [15,17].

In volume coupling, the changes in pore volume occur in response to variations in stress, pressure, and temperature. For convergence, the calculated pore volume changes should be the same in both the fluid flow model and the geomechanical model. The pore volume changes of the geomechanical model are usually more accurate than those of the fluid flow model because they are calculated by volumetric strain via a more realistic complex material constitutive model. This method is well suited to shear and plastic deformation, which involve large changes in pore volume or porosity. These problems are common in unconsolidated heavy oils and oil sands, North Sea chalk, Californian diatomite, and possibly some other materials [15,17].

In case of fluid flow coupling, the changes in permeability and relative permeability are related to the changes in stress, shear stress, and compaction. Material parameters, such as permeability, relative permeability, compressibility, and others, change when conditions encounter a shear fracture. This fact is important in some reservoirs where the rock compressibility does not play a significant role in volumetric behaviour, such as gas reservoirs where volume coupling is not important. Another example is cold water/fluid injection, which leads to a thermally-induced decrease in horizontal stress until the injection pressure increases the minimum horizontal stress [19].

To achieve the stress states of the reservoir and surrounding formations throughout history, as well as during future gas storage operations, the fluid flow and the geomechanical simulation must be coupled. The pore pressure controls the effective stresses and, hence, deformation, in turn changing rock porosity and permeability, which again affect fluid flow.

### 2.3.1. Effective Stress and Poroelasticity

The effective stress for incompressible rock and the concept of one-dimensional consolidation are the fundamentals of poroelasticity formulated by Terzaghi in 1923 [17]. Successively, using the basic principles of continuum mechanics and applying the concept of the coupling of stress and pore pressure in a porous medium, Biot developed a comprehensive three-dimensional theory of consolidation [17,20]. Biot's theory and the papers that he published are more aligned towards geomechanics than flow models, due to which they are rarely compatible with the coupling of geomechanics and flow models. By introducing the so-called Skempton pore pressure parameters (A and B), Skempton in 1954 procured a relationship between the total stress and the pore pressure under undrained initial loading [17,21]. Later, however, the relationships among pore pressure, stress, and volume and the concept of compressibility in a porous medium were better clarified by Geerstma in 1957 [17,22]. Later, Van der Knaap (1959) extended Geerstma's work to nonlinear elastic geomaterials only for dense and uncemented sands [17,23]. By applying Biot's theory, Geerstma in 1966 examined subsidence problems in oil fields and published prototype geomechanical modelling, which is probably the first-ever coupled analysis of fluid flow [17,20]. Nur and Byerlee (1971) demonstrated that the effective stress law proposed by Biot is far more general and precise than that proposed by Terzaghi [17,24]. Nevertheless, there are certain limitations (one-dimensional analysis, neglect of the compressibility of

fluids and rocks, etc.) that Terzaghi recognized in the assumptions that he made in the 1920s to solve problems of applied rock mechanics in clay consolidation [17]. Later in the 1970s, there were further developments on coupled flow stress issues; e.g., fluid compressibility was introduced into the classical soil mechanical consolidation theory of Ghaboussi and Wilson [17,25]. Rice and Cleary (1976) showed how poroelasticity problems could be solved using pore pressure and stress as primary variables, instead of the displacements used by Biot [17,26].

### 2.3.2. Simulation Concept and Governing Equations

The numerical modelling of an underground gas reservoir can contribute to the understanding of the interaction mechanisms between the injected gas and the deformation of the reservoir. The injection of cold foreign gas into the reservoir leads to thermal and mechanical disequilibrium in the reservoir by altering the transport properties, including porosity and permeability. A three-dimensional THM coupling model of a reservoir is created by incorporating the mechanical equilibrium equation, the fluid flow or seepage equation (Darcy equation), the heat transfer equation (Fourier equation) of the formation's rock matrix, and the THM stress equation. These equations are based on the porosity, permeability, thermal diffusivity, and other physical and mechanical parameters of the sandstone formation [27].

The mechanical equilibrium equation can be expressed as follows [27]:

$$S_{i,j,j} + f_i = 0, \quad (3)$$

where,  $S_{i,j,j}$  is the total stress tensor ( $\text{N}/\text{m}^2$ ), and  $f_i$  is the body force ( $\text{N}/\text{m}^3$ ). The equation of the continuity of the fluid flow in the rock can be written as [27]:

$$\frac{\partial \rho_l}{\partial t} + \frac{\partial(\rho_l v_r)}{r \partial r} + \frac{\partial(\rho_l v_\theta)}{r \partial \theta} + \frac{\partial(\rho_l w)}{\partial z} = 0, \quad (4)$$

In this equation  $v_r$ ,  $v_\theta$ , and  $w$  are the Darcy velocities ( $\text{m}/\text{s}$ ) along the radial, hoop, and well-depth directions, respectively, in the porous reservoir. The relationship between stress and porosity/permeability changes in porous rock can be described with the following equations [27,28],

$$\phi = \phi_r + (\phi_0 - \phi_r) \exp(e S_M), \quad (5)$$

$$k = k_0 \exp(c \cdot (\frac{\phi}{\phi_0} - 1)), \quad (6)$$

In the above equations,  $S_M$  denotes mean effective stress;  $\phi_0$  and  $k_0$  are the porosity and permeability at zero stress, respectively;  $\phi_r$  represents the residual porosity at high stress; and the exponents  $e$  and  $c$  are determined experimentally.

The heat transfer process and the total energy conservation can be express by rewriting the Fourier equation [29]:

$$(\rho c)_t \frac{\partial T}{\partial t} - \frac{1}{r} \frac{\partial}{\partial r} (k_t r \frac{\partial T}{\partial r}) - \frac{1}{r^2} \frac{\partial}{\partial \theta} (k_t \frac{\partial T}{\partial \theta}) - \frac{\partial}{\partial z} (k_t \frac{\partial T}{\partial z}) - q_t r = 0, \quad (7)$$

$$(\rho c)_t = (1 - \phi) c_s \rho_s + \phi c_f \rho_f, \quad (8)$$

$$k_{total} = \phi k_f + (1 - \phi) k_s, \quad (9)$$

In the above equations, the total heat capacity of the solid and fluid phases is denoted by  $(\rho c)_t$  in units ( $\text{J}/(\text{m}^3 \cdot ^\circ\text{C})$ );  $k_{total}$  is the total thermal conductivity ( $\text{J}/(\text{m} \cdot \text{s} \cdot ^\circ\text{C})$ );  $q_t$  is the intensity of the internal heat source ( $\text{J}/(\text{m}^3 \cdot \text{s})$ );  $c_s$  and  $c_f$  are the specific heat capacities of the formation and the fluid, respectively ( $\text{J}/\text{kg} \cdot \text{K}$ );  $\rho_s$  and  $\rho_f$  are the density of the formation

and the fluid ( $\text{Kg}/\text{m}^3$ ), respectively; and  $k_s$  and  $k_f$  are the thermal conductivity of the formation and the fluid ( $\text{W}/(\text{m}\cdot\text{K})$ ), respectively [29].

Finally, the governing equation involving all important thermal-hydro-mechanical parameters is as follows [30]:

$$2\alpha \frac{(1-2\nu)}{1+\nu} \nabla^2 p + 6\beta K_B \frac{(1-2\nu)}{1+\nu} \nabla^2 T - \nabla \cdot f - 3 \frac{(1-\nu)}{1+\nu} \nabla^2 S_{m(\text{total})} = 0, \quad (10)$$

where  $S_{m(\text{total})}$  is the mean total stress (MPa),  $\nu$  is the Poisson's ratio of the rock mass,  $\alpha$  is the Biot coefficient,  $\beta$  is the coefficient of linear thermal expansion ( $1/^\circ\text{C}$ ), and  $K_B$  is the bulk modulus of the rock (MPa). The term  $(2\alpha \frac{(1-2\nu)}{1+\nu} \nabla^2 p)$  describes the effect of poroelastic stress;  $(6\beta K_B \frac{(1-2\nu)}{1+\nu} \nabla^2 T)$  represents thermalelastic stress; and the term  $(\nabla \cdot f - 3 \frac{(1-\nu)}{1+\nu} \nabla^2 S_{m(\text{total})})$  shows the body force [30].

#### 2.4. ECLIPSE<sup>TM</sup>\_VISAGE<sup>TM</sup> THM Modelling

The THM modelling is performed using two commercial software packages, referred to here as the ECLIPSE<sup>TM</sup>-VISAGE<sup>TM</sup> coupling. ECLIPSE<sup>TM</sup> is a conventional reservoir simulator used as the flow simulator for the multiphase flow processes. In the following study, the ECLIPSE<sup>TM</sup> 100 finite difference black oil simulator is used for the flow calculations. VISAGE<sup>TM</sup> is one of the most advanced and comprehensive stress analysis simulators commercially available. It is designed for applications in which nonlinear mechanics play a greater role, for example, in disciplines such as rock mechanics and geomechanics. It is flexible and can also be used in many other scientific disciplines, e.g., fluid mechanics, heat transfer, materials science, etc. The system provides high computational power and sophisticated modelling for many analytical situations, which currently include mining, civil engineering, reservoir engineering, and geothermal energy.

The advanced and comprehensive finite element code (VISAGE<sup>TM</sup>) has been coupled with the ECLIPSE<sup>TM</sup> reservoir simulator to include geomechanical processes in this modelling study. Fluid flow is first calculated in ECLIPSE<sup>TM</sup>, and the results are then transferred from ECLIPSE<sup>TM</sup> to VISAGE<sup>TM</sup> via the ECL2VIS interface for specified time steps. Updates of porosity and permeability can be calculated via constitutive relations, e.g., Kozeny–Carman.

The coupled THM models are based on three fundamental laws, namely Hooke's law of elasticity, Fourier's law of heat conduction, and Darcy's law of fluid flow in porous media. The governing equations are discussed above.

One-way coupling is usually sufficient for THM modelling of gas reservoirs, as gas compressibility dominates the bulk rock compressibility, and the mass balance is mainly controlled by gas pressure rather than by the stresses of solid rock [31]. The THM-coupled model presented in this paper is a one-way coupled model. With this approach, pressure data are transferred from the reservoir simulator (fluid flow simulator) ECLIPSE<sup>TM</sup> to the mechanical finite element simulator (geomechanical simulator) VISAGE<sup>TM</sup> at regular and/or critical times. The fluid pressure drives the geomechanics, but mechanically induced changes in porosity and permeability are not fed back into the dynamic reservoir simulation. It is therefore assumed that permeability and porosity are the same for each time step in the modelling and are not influenced by changes in stresses or ageing effects of the reservoir. This type of approach is feasible in this case study due to the high permeability of up to 80 mD, which is characteristic of the reservoir.

### 3. Case Study

The presented modelling study is a working example of how to set up and populate a 3D coupled thermal-hydraulic-mechanical model of an underground gas storage site. The case study reservoir is a depleted gas reservoir located about 65 km east of Munich in the Central Molasse Basin. It is an anticlinal structural trap bounded by a normal fault. The reservoir formation is mainly Early Cenozoic Chattian sand, with 85-m thick, three gas-

bearing layers, found at a depth of 1770 m (1200 m below sea level). The initial gas-water contact is at 1239 m below sea level (BSL). The reservoir has produced 528 million m<sup>3</sup> of gas over 18 years from 1958 till 1976; replenishment started in 1978 and has continued to the present, and the reservoir has not been in operation to date [10]. The modelling study uses pore pressure development during the production history and subsequent shut-in phase to calibrate the dynamic reservoir fluid model.

The 3D MEM model is built using a hydraulic model (green area in Figure 1), which comprises a high-resolution reservoir section and regions of lower resolution away from the reservoir section, called the sideburden, overburden, and underburden sections. Topography is extracted from the elevation maps of the ground level to include the top surface of the model. The horizons bounding the reservoir are used to make overburden layers and underburden layers. The basal unit of the model comprises crystalline basement rocks at a depth of about 5 km. However, as none of the wells has reached this depth, this information is inferred from regional geological knowledge. The final 3D THM model consists of 12 horizons and 11 lithostratigraphic units with dimensions of about 30 × 24 × 5 km<sup>3</sup> in the X, Y, and Z directions, respectively. The grid of the THM with the reservoir model embedded is shown in Figure 1. The higher resolution in the area of interest (reservoir) and the lower resolution outside make up a grid that creates balance between simulation precision and computational demand. The initial pore pressures and elastic properties are upscaled and interpolated from the 1D MEM's. The calculated and calibrated log-derived properties, including pore pressure, Young's modulus, Poisson's ratio, and density, are upscaled from the well locations to the entire model domain. The Kriging interpolation method is used to populate the 3D geomechanical model. The precision is of course decreasing away from the wells, but the model fits well with overall trends.

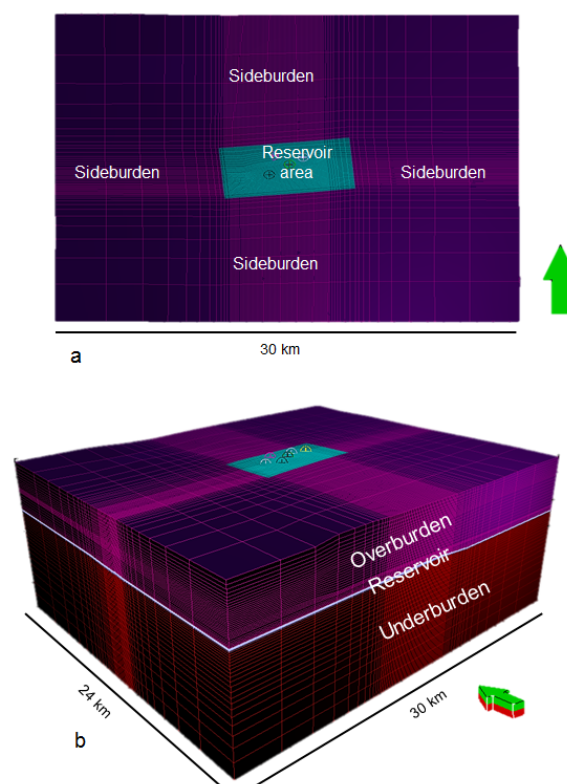


**Figure 1.** Reservoir model proper embedded in 3D geomechanical model with reservoir, overburden, underburden, and sideburden zones: (a) is the top view, and (b) is the oblique view, the arrows represent north direction [10].

Further details regarding the model setup, population of the model from 1D MEMs, history match, etc., are explained in our previous publication [10]. The starting point of the

further modelling study in the following sections is the state after the replenishment phase, achieved by a history match of the production and pressure data from the production and subsequent shut-in phases, respectively.

## 4. Modelling

### 4.1. Modelling Scenarios

The following section describes the dynamic fluid flow models setup for future scenario testing cases designed for short-term (weekly) gas storage operations. The pressure profile of different future testing scenarios can be coupled with and incorporated into the THM model. The concept for these scenario tests is to evaluate geomechanical stresses on the reservoir due to pressure changes with intensive injection/production cycles. There are various models with different short-term cases that have been considered. German data for excess electricity throughout 2017 have also been considered in one case to address the issues of renewable energy aspects. This case implies that the excess of power energy (electricity) in Germany can be stored in underground gas storage with the power-to-gas (PtG) concept, and then the stored gas can be reused for power generation (gas-to-power) when needed. All the cases are summarized in Table 1. The starting pressure point of these future scenario testing cases is the end point pressure of the replenishment phase, i.e., ~15.8 MPa.

**Table 1.** All modelling scenarios with input parameters. WBHP is well bottom hole pressure, WGIR is well gas injection rate, and WGPR is well gas production rate.

Modelling Scenarios	Subdivisions	Input Parameters				
		WBHP upper limit (MPa)	WBHP lower limit (MPa)	WGIR (m <sup>3</sup> /day)	WGPR (m <sup>3</sup> /day)	
Short-term (weekly) cases	Case A (with water-cut 5 m <sup>3</sup> /day)	With three wells (two vertical wells, one horizontal well)	18.8	13.8	100,000	100,000
	Case B (without limited water-cut)	With three wells (two vertical wells and one horizontal well)	18.8	13.8	100,000	100,000
Real-world cases	Case C (with water-cut 5 m <sup>3</sup> /day)	With one well	18.8	13.8	100,000	100,000
	Case D (without limited water-cut)	With one well	18.8	13.8	100,000	100,000

Short-term scenario cases represent weekly storage operations. The scenario scheme has been designed to compensate for the excess power produced in a season and to store power-to-gas energy into same underground gas storage. A short-term cycle consists of phases of one week of injection, one week of shut in, two weeks of production, and one week of shut (1wkInj-1wkShut-2wkProd-1wkShut) for one year. During the injection week, gas is injected into the reservoir, which builds up field pressure (but again limited by 18.8 MPa, the upper limit of WBHP); then, one week of shut in maintains the pressure, followed by a two-week production phase to withdraw gas, which drops the field pressure (lower limit constraint to 13.8 MPa), and again a shut in phase to maintain the well bore pressure.

#### 4.2. Case A

There are three wells considered for this scenario: two wells are vertical wells (X2 and X6), and one is a horizontal well (H1). All the wells have been considered to have the same short-term weekly schedule as discussed above. This case comprises the same schedule as discussed above, but the well water production rate (WWPR) is limited to 5 m<sup>3</sup>/day to take into consideration the economic aspects of operating the gas storage. The commercial storage industry limits the water production rates to minimize operating costs and enhance economic returns. Therefore, this aspect has also been considered in this case study. The gas rate for injection and production both is 100,000 m<sup>3</sup>/day. Bottom hole pressure is constrained by an upper limit of 18.8 MPa and a lower limit of 13.8 MPa in cases of injection and production, respectively. The water cut-off is again 5 m<sup>3</sup>/day in the production phase to limit the production of water from each well.

The FPR profile for this case is shown in Figure 2. The progressive oscillation cycles of FPR are injection (upward) and production (downward) phases. The overall upward trend of FPR from its initial pressure of ~15.39 MPa represents the buildup pressure with each passing schedule cycle.

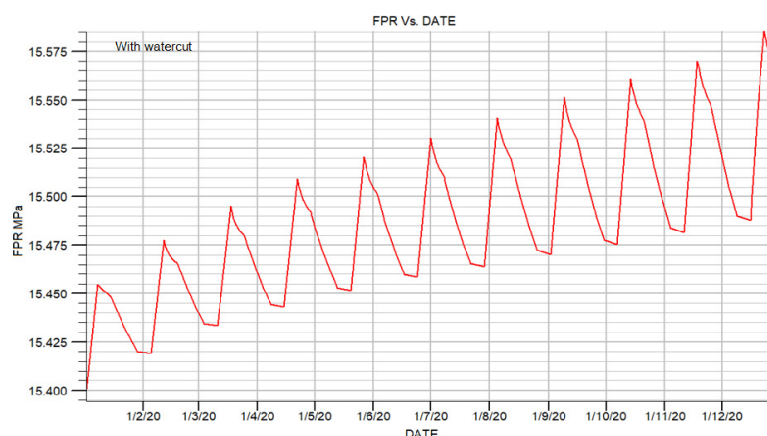


**Figure 2.** Field pressure (FPR) profiles of all three wells (X2, X6, and H1) with schedule 1wkInj-1wkShut-2wkProd-1wkShut for one year.

The upward trend of FPR throughout the schedule year is due to the well water production rate (WWPR) (Figure 3d), and as a result, the field pressure is not stabilized in such a short time span. To maintain material balance in this scenario, the injection rate should be lowered to the actual production rates of each cycle.

The comparison of the properties of all three wells is summarized in Figure 3. The WBHP of X6 reaches the maximum limit of 18.8 MPa at the end of each injection cycle and drops back to ~15 MPa at the end of the production phase. The WBHP of X2 also shows similar behaviour but at a lower pressure; e.g., it varies between 16 MPa and 17 MPa at the end of each injection phase and drops back to the same level of ~15 MPa. The WBHP behaviour of H1 is however different from that of both X2 and X6. It reaches a maximum value of 16 MPa at the peak injection time and drops to the lowest level of ~14 MPa (Figure 3a). The WGPR behaviour of all three wells is similar with respect to linear increases with each increasing cycle. However, the rates are completely different for each well. The WGPR of well X2 ranges within ~10,000–11,000 m<sup>3</sup>/day during the initial cycles but reaches up to 18,000 m<sup>3</sup>/day at the end of the schedule. Contrarily, the WGPR of well X6 ranges within ~5000–6000 m<sup>3</sup>/day during the initial cycles but reaches up to ~9000 m<sup>3</sup>/day at the last cycle. An entirely different behaviour of WGPR is exhibited by well H1, showing ~50 m<sup>3</sup>/day during the initial cycles but reaching up to ~1100 m<sup>3</sup>/day at the end of the schedule year (Figure 3b).

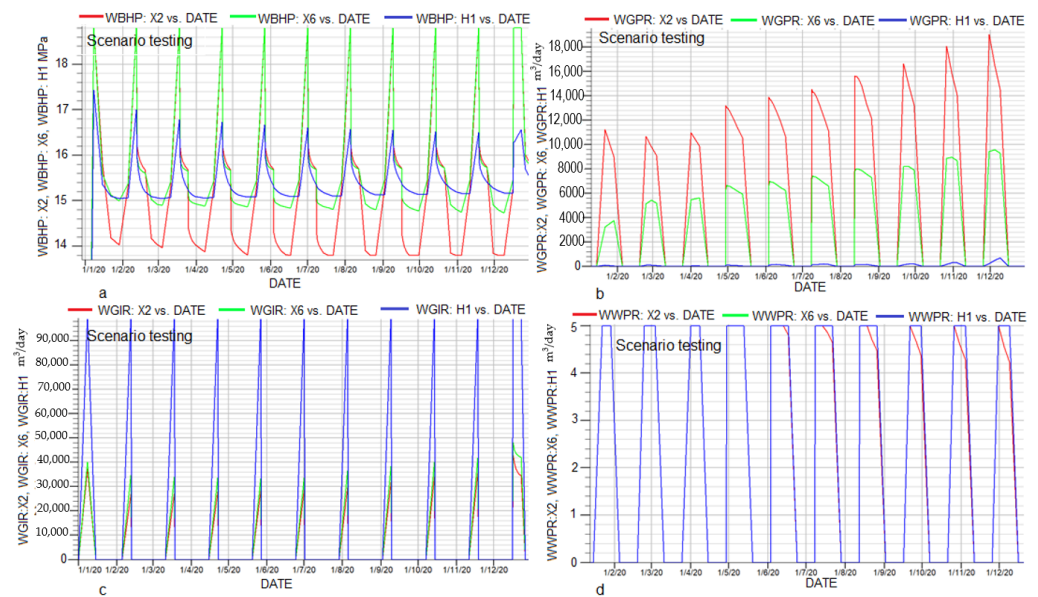


**Figure 3.** Well properties comparison of the three-well case scenario with the short-term schedule 1wkInj-1wkShut-2wkProd-1wkShut for one year. X2 and X6 are vertical wells, and H1 is the horizontal well: (a) well bottom hole pressure (WBHP) of all wells; (b) production gas rates (WGPRs) for all three wells; (c) injection gas rates (WGIRs) for all three wells and; (d) well water production rate (WWPR) for all the wells.

The WGIR profile of each well is completely different from the profile of the WGPR; the WGIR of well H1 shows the highest WGIR rates among other vertical wells (X2 and X6). The WGIR of H1 reaches to the maximum rate of  $100,000 \text{ m}^3/\text{day}$ . The WGIR of well X2 and X6 reach a maximum of  $40,000 \text{ m}^3/\text{day}$  and  $50,000 \text{ m}^3/\text{day}$ , respectively (Figure 3c).

The comparison shows that the horizontal well allows more gas injection and less gas production than the vertical wells and vice versa.

## Results

The modelling results of this case are presented in the form of pore pressure and effective stress changes of the top layer of the reservoir. Two-time steps have been selected for the analyses of changes in pore pressure and effective stresses acting on the reservoir. Time step t1 (16 December 2020) represents the lowest pressure during the production phase of the schedule cycle, and t2 (23 December 2020) indicates the maximum injection pressure. The fluctuations in pore pressure and effective stress on the reservoir during t1 and t2 are the main results of this model.

Figure 4 shows the locations of three wells, which are denoted by H1, X2, and X6. The pore pressures at t1 and t2 for the well H1 are  $\sim 15.0 \text{ MPa}$  and  $\sim 15.3 \text{ MPa}$ , respectively, whereas the effective stress values are  $\sim 29.3 \text{ MPa}$  at t1 and about  $29.0 \text{ MPa}$  at t2. There is a difference of about  $\sim 0.3 \text{ MPa}$  for both pore pressure and effective stress from t1 to t2.

The vertical wells X2 and X6 are close to each other; therefore, the differences in the change in pore pressure and effective stress at these well locations are negligible. The values of pore pressure at both well locations at t1 and t2 are about  $15.4 \text{ MPa}$  and  $\sim 15.7 \text{ MPa}$ , respectively. The effective stresses at t1 and t2 are  $\sim 28.5$  and  $\sim 28.2 \text{ MPa}$ , respectively, at both well locations. There is an increase in pore pressure of  $\sim 0.3 \text{ MPa}$  from t1 to t2 and a decrease in effective stress of about  $0.3 \text{ MPa}$ .

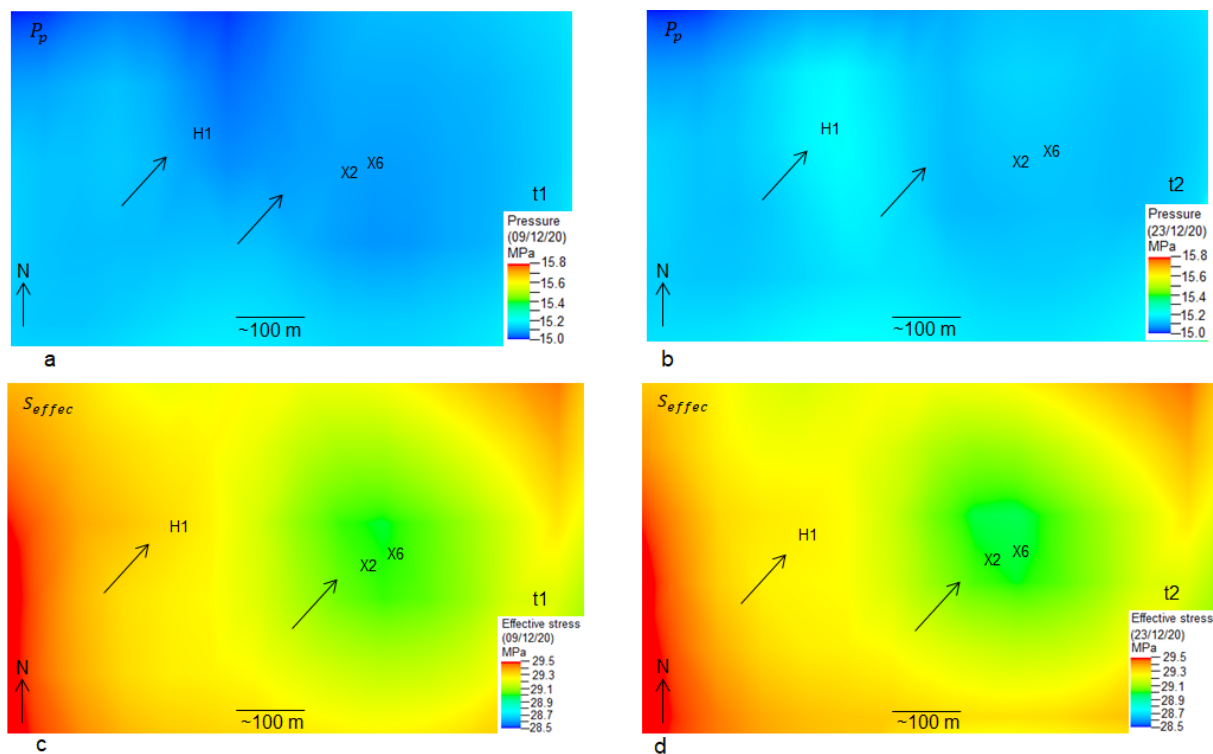


**Figure 4.** Pore pressure ( $P_p$ ) and effective stress ( $S_{effec}$ ) changes from t1 (16 December 2020) to t2 (23 December 2020) in the short-term case with three wells (X2, X6, and H1) with a water cut-off rate of  $5 \text{ m}^3/\text{day}$ . The arrows show the location of maximum observed fluctuations in  $P_p$  and  $S_{effec}$  from t1 to t2. The color scale is in MPa. (a) is pore pressure at time t1; (b) is pore pressure at time t2; (c) is effective stress at time t1; (d) is effective stress at time t2.

#### 4.3. Case B

Three wells are considered for this scenario, two of which are vertical wells (X2 and X6), and one is a horizontal well (H1). All wells are assumed to have the same short-term weekly schedule as described above. WGIR and WGPR both have same value of  $100,000 \text{ m}^3/\text{day}$ ; however, they are constrained by the upper limit of BHP of 18.8 MPa and the lower limit of BHP of 13.8 MPa in the cases of injection and production, respectively.

The FPR profile for this case is shown in Figure 5. The progressive oscillation cycles of the FPR are injection (upward) and production (downward) phases. The general trend of the FPR remains within the limits of  $\sim 15.85 \text{ MPa}$  and  $\sim 15.375 \text{ MPa}$  during the injection and production phases, respectively.

The comparison of the properties of all three wells is summarized in Figure 6. The WBHP of X6 reaches the maximum limit of 18.8 MPa at the end of each injection cycle and falls back to  $\sim 13.8 \text{ MPa}$  at the end of the production phase. The WBHP of X2 also shows almost similar behaviour. However, the WBHP behaviour of H1 is different from both X2 and X6. It reaches a maximum value of 17.4 MPa at peak injection time and drops to the lowest level of  $\sim 13.8 \text{ MPa}$  (Figure 6a). The WGPR behaviour of all three wells is similar in terms of linear increase with each increasing cycle. However, the rates are completely different for each well. The WGPR of well X2 is  $\sim 12,000\text{--}16,000 \text{ m}^3/\text{day}$  during the initial cycles but reaches up to  $24,000 \text{ m}^3/\text{day}$  at the end of the schedule. In contrast, the WGPR of well X6 varies between  $14,000$  and  $15,000 \text{ m}^3/\text{day}$  during the initial cycles and reaches up to  $22,000 \text{ m}^3/\text{day}$  at the end of the last schedule cycle. The WGPR of well H1 is entirely different from the other two wells because it shows  $\sim 400\text{--}500 \text{ m}^3/\text{day}$  during the initial cycles but reaches up to  $\sim 70,000 \text{ m}^3/\text{day}$  at the end of the schedule year (Figure 6b).

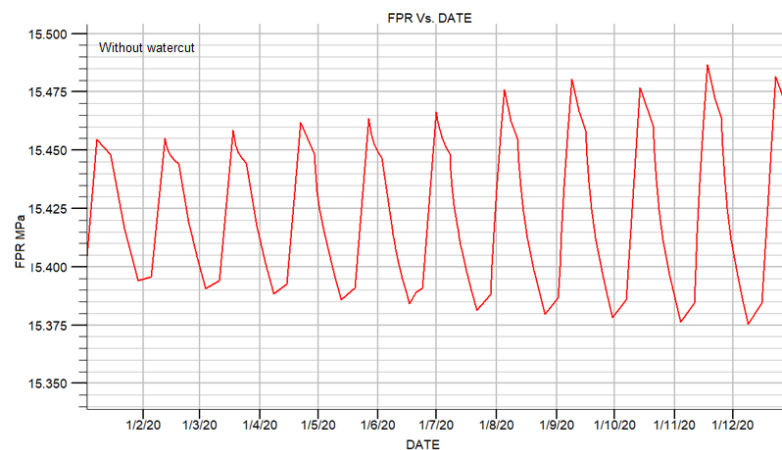


**Figure 5.** Field pressure (FPR) profile of all three wells (X2, X6, and H1) with schedule 1wkInj-1wkShut-2wkProd-1wkShut for 1 year.

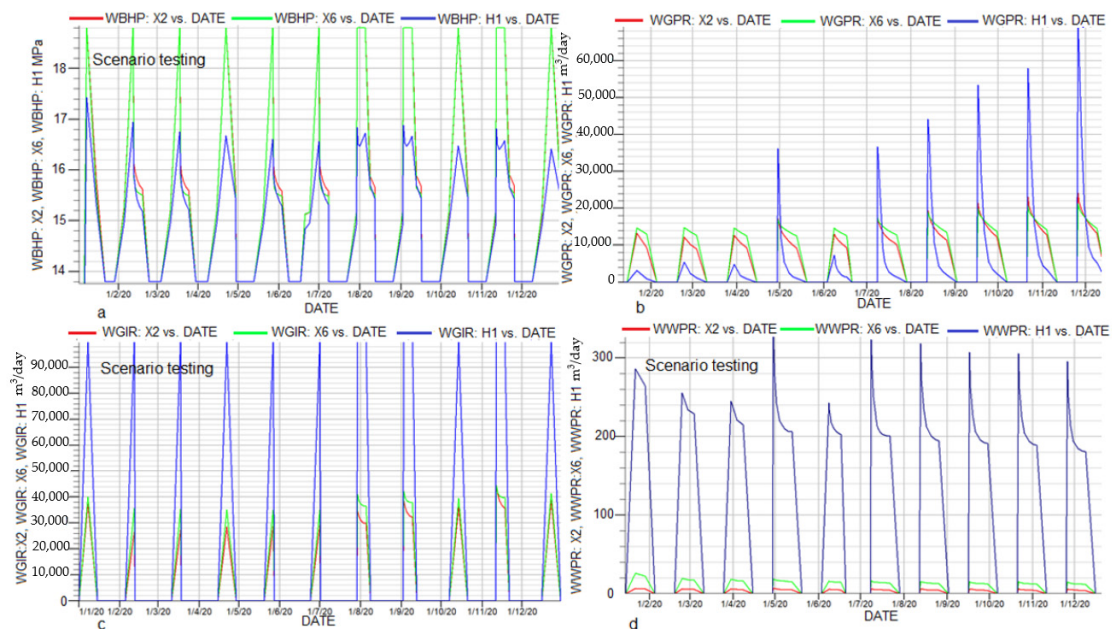


**Figure 6.** Well properties comparison of the three-well case scenario with short-term schedule 1wkInj-1wkShut-2wkProd-1wkShut 1 year. X2 and X6 are vertical wells, and H1 is the horizontal well: (a) well bottom hole pressure (WBHP) of all wells; (b) production gas rate (WGPR) for all three wells; (c) injection gas rate (WGIR) for all three wells and; (d) well water production rate (WWPR) for all the wells.

The WGIR profile of each well is completely different from the WGPR profile; the WGIR of well H1 shows the highest WGIR among the other vertical wells (X2 and X6). The WGIR of well H1 reaches the maximum value of  $100,000 \text{ m}^3/\text{day}$ . The WGIRs of wells X2 and X6 reach maximum values of  $44,000 \text{ m}^3/\text{day}$  and  $45,000 \text{ m}^3/\text{day}$ , respectively (Figure 6c). The comparison shows that the horizontal wells allow for higher WGIR and WGPR than the vertical wells under the same WBHP conditions.

The WWPR of well X2 allows a maximum rate of  $5 \text{ m}^3/\text{day}$  throughout schedule year, and the WWPR of well X6 also remain constant over the schedule year with a rate of  $10 \text{ m}^3/\text{day}$ , while the WWPR of well H1 remains higher, within the range of  $250 \text{ m}^3/\text{day}$  to  $310 \text{ m}^3/\text{day}$  (Figure 6d).

#### 4.3.1. Results

The modelling results of this case are presented in the form of pore pressure and effective stress changes of the top layer of the reservoir. Two time steps with the greatest fluctuations in pore pressure have been selected. Time step t1 (9 December 2020) corresponds to the lowest pore pressure point, and t2 (23 December 2020) corresponds to the highest pore pressure point of the schedule cycle. The fluctuation in pore pressure and the effective stress on the reservoir during time t1 and t2 are the main results of this model.

Figure 7 shows the locations of three wells, which are denoted by H1, X2, and X6. These three wells are the operating wells for this scenario. The main changes in pore pressure, along with the effective stress, occur around these wells. The pore pressures at t1 and t2 for well H1 are ~15.5 MPa and ~15.4 MPa, respectively, whereas the effective stress values are ~29.1 MPa at t1 and about ~28.7 MPa at t2. There is a difference of about ~0.4 MPa for both pore pressure and effective stress at t1 and t2.

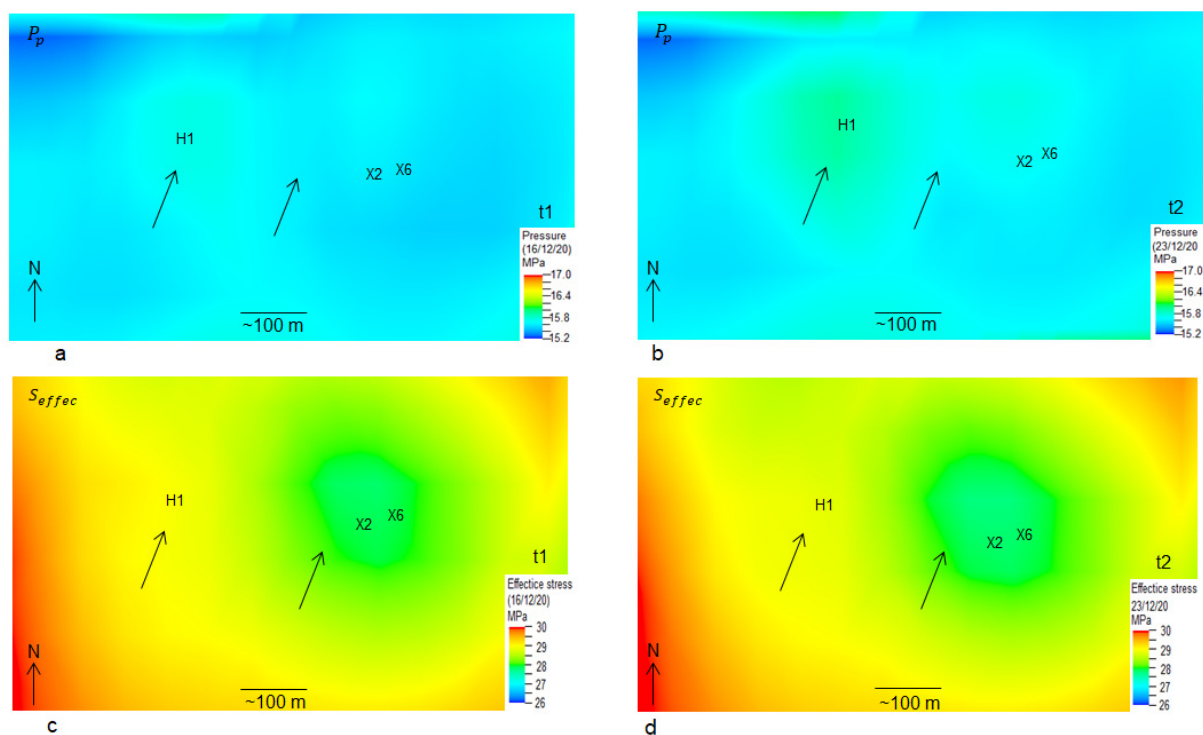


**Figure 7.** Pore pressure ( $P_p$ ) and effective stress ( $S_{effec}$ ) changes from t1 (9 December 2020) to t2 (23 December 2020) in the short-term case with three wells (X2, X6, and H1) without a water cut-off rate of  $5 \text{ m}^3/\text{day}$ . The arrows show the location of maximum observed changes in  $P_p$  and  $S_{effec}$  from t1 to t2. The color scale is in MPa. (a) is pore pressure at time t1; (b) is pore pressure at time t2; (c) is effective stress at time t1; (d) is effective stress at time t2.

#### 4.3.2. Real World Cases

The excess of electricity produced [32,33] in Germany could be stored in underground gas storage by converting the power energy into gas (Power-to-Gas). PtG is a process of generation of a gas with high energy density through the electrolysis of water. The first intermediate product is power-to-hydrogen, which can be converted into synthetic methane gas power-to-methane in a subsequent methanation process that requires injection of  $\text{CO}_2$ . In this way, the same seasonal underground gas storage can also be used as a battery for excess energy in a calendar year. Figure 8 shows Germany's data on excess electricity produced in calendar year 2017. It can be seen from the data that, during the summertime (from March till August), electricity produced from renewable sources, such as wind and solar, increases enormously. The combined wind energy (onshore and offshore) shows high variation during the first and fourth quarters of the year, meaning this high variation of

electricity production from renewable sources can be stored (power-to-gas) and reused (gas-to-power) in cases of excesses and shortages of electricity, respectively.

### Stromerzeugung und Stromverbrauch 2017

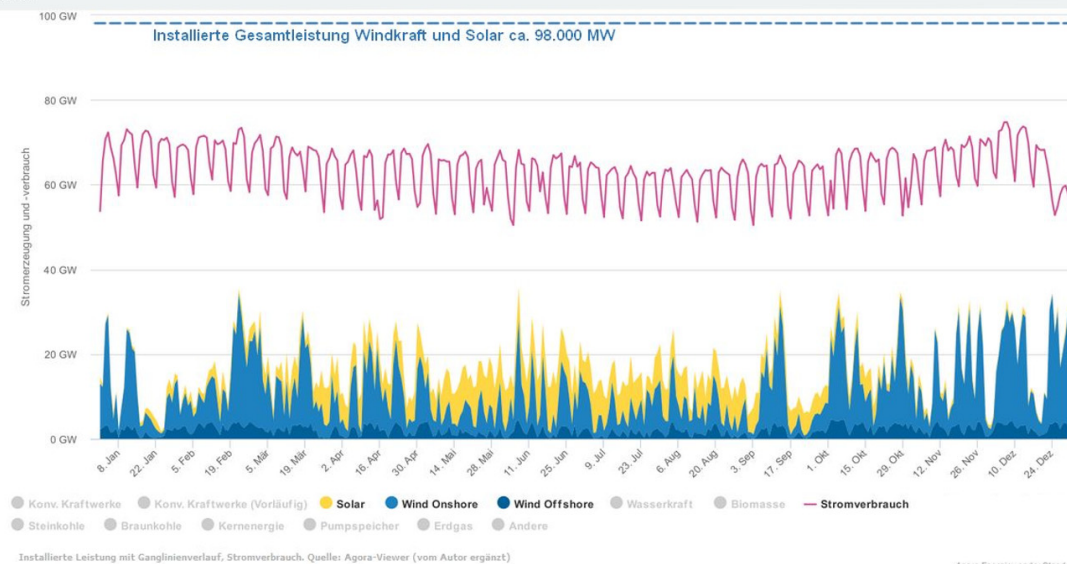


**Figure 8.** Data show the consumption of total electricity in Germany, along with electricity produced from renewable energy sources (such as wind, either offshore or onshore, and solar) in calendar year 2017 [32,33].

These scenarios have been performed on well X6. The schedule is based on the data shown in Figure 8. The baseline of 10 GW is the shut-in period. Greater than the 10-GW baseline is considered to have an excess of electricity that can be used as injection periods for power-to-gas storage, and less than the limit of 10 GW is a shortage of electricity. These periods have been considered for the production of gas for gas-to-power conversion. These data [32,33] on excess electricity from Germany have been used to conduct two short-term real world case schedule cases: one with limited water cut-off and one without limited water cut-off.

#### 4.4. Case C

This scenario has been performed on vertical well X6. The schedule timeline of one year has been adopted from Figure 8. The well water production rate (WWPR) is restricted to 5 m<sup>3</sup>/day (Figure 9c). The FPR eventually increases in this case to up to 15.72 MPa with slight variations during the gas production cycles. Gas injection succeeds to maintain the pressure, and it increases from ~15.39 MPa and reaches approximately ~15.72 MPa at the end of the one-year period (Figure 9a). The variability in WBHP is directly proportional to the gas production cycles. As shown in Figure 9a, as the gas production increases, the well bottom-hole pressure decreases even as the gas injection continues. The maximum WBHP reaches a value of 18.8 MPa, the minimum WBHP reaches a value of 14.4 MPa, and these maximum and minimum pressure values represent injection and production cycles (Figure 9b). The well gas injection rate (WGIR) varies during the year, having a minimum injection rate of approximately 32,000 m<sup>3</sup>/day and a maximum rate of about 66,000 m<sup>3</sup>/day. In contrast, the well gas production rate (WGPR) has minimum and maximum values of 4300 m<sup>3</sup>/day and 19,000 m<sup>3</sup>/day, respectively (Figure 9d). The lower WGPR compared to the WGIR is due to the limited WWPR, which does not allow the well to produce at a higher WGPR.

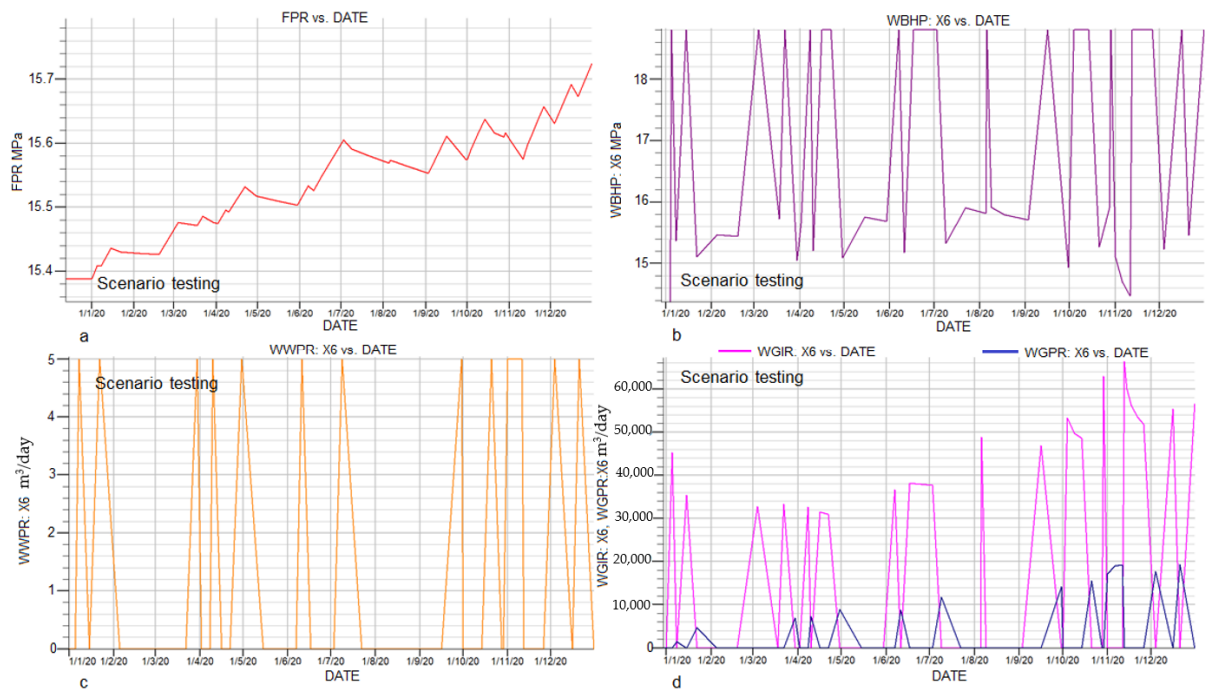


**Figure 9.** The fluctuation in electricity produced in Germany from renewable sources in 2017 is modelled into a future scenario testing case with limited water cut-off ( $5 \text{ m}^3/\text{day}$ ). The excess of energy can be stored in UGS and can be used when needed. This schedule is helpful to understand in which month of the year energy can be stored as gas in UGS and in which month of the year this energy can be utilized when shortage occurs: (a) field pressure (FPR) profile for these cycles; (b) well bottom hole pressure (WBHP) of well X6; (c) well water production rate (WWPR) for well X6; and (d) well gas injection rate (WGIR) and well gas production rate (WGPR) for well X6.

**Results**

The modelling results of this case are presented in the form of the pore pressure and effective stress changes in the top layer of the reservoir. Two time steps have been selected for the conclusion of the results for this model. Time step t1 is the starting point of the schedule case, i.e., 1 January 2020, and t2 is the end schedule point (31 December 2020). The pore pressure at the well X6 location is about 15.2 MPa at t1 and increases to about 15.8 MPa at t2; simultaneously, the effective stresses at well X6 is about 28.6 MPa, and it decreases to about 28.0 MPa at time steps t1 and t2 (Figure 10). There is an increase of 0.6 MPa in pore pressure and decrease of 0.6 MPa in effective stress at the top surface of the reservoir layer near well X6 from t1 to t2.

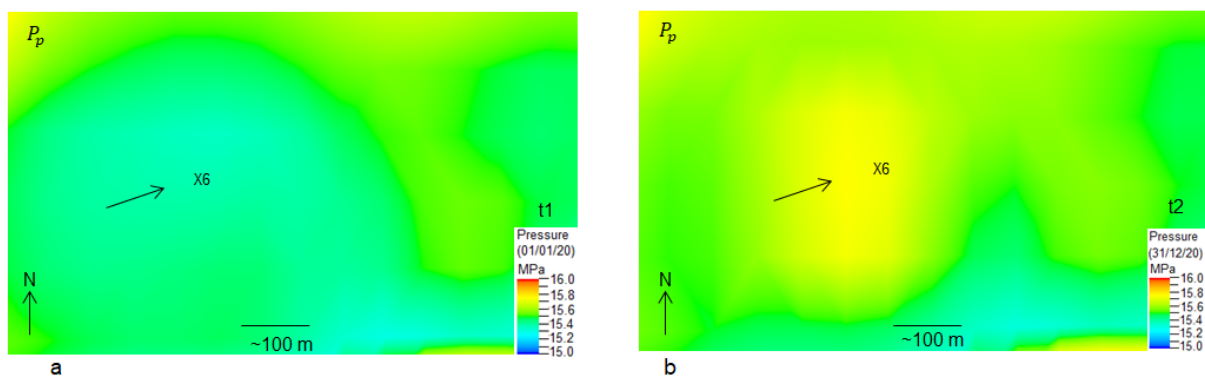


**Figure 10. Cont.**

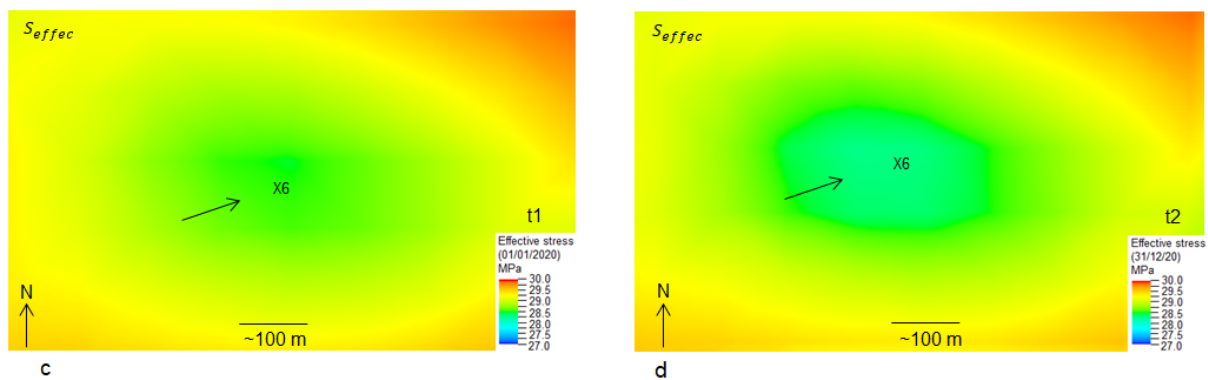


**Figure 10.** Pore pressure ( $P_p$ ) and effective stress ( $S_{effec}$ ) changes from t1 (1 January 2020) to t2 (31 December 2020) in the short-term case with one well (X6) with a water cut-off rate of  $5 \text{ m}^3/\text{day}$  and a random schedule. The arrows show the location of the maximum observed fluctuation in  $P_p$  and  $S_{effec}$  from t1 to t2. The color scale is in MPa. (a) is pore pressure at time t1; (b) is pore pressure at time t2; (c) is effective stress at time t1; (d) is effective stress at time t2.

#### 4.5. Case D

This scenario has been performed on vertical well X6. The schedule timeline of one year has been adopted from Figure 8. There was no water cut-off rate limit set in this scenario; hence, the maximum water production rate (WWPR) increases up to  $43 \text{ m}^3/\text{day}$  and remains less than  $20 \text{ m}^3/\text{day}$  throughout the production and injection period of one year, respectively (Figure 11c). The FPR is sustained in this case by gas injection and increases to up to a maximum value of 15.62 MPa with slight variation during the gas production cycles in the one-year period (Figure 11a). The alteration in WBHP is directly proportional to the gas production cycles without a water cut-off limit. As shown in Figure 11b, the WBHP reaches a maximum value of 18.8 MPa and a minimum value of approximately 13.8 MPa. The well gas injection rate (WGIR) varies during the year, having a minimum injection rate of approximately  $32,000 \text{ m}^3/\text{day}$  and a maximum rate of about  $60,000 \text{ m}^3/\text{day}$ , whereas the well gas production rate (WGPR) has minimum and maximum values of  $16,000 \text{ m}^3/\text{day}$  and  $40,000 \text{ m}^3/\text{day}$ , respectively (Figure 11d).

#### Results

The modelling results of this case are presented in the form of pore pressure and effective stress changes of the top layer of the reservoir. Two time steps have been selected for the conclusion of the results for this model. Time step t1 is the starting point of the schedule case, i.e., 1 January 20, and t2 is the end schedule point (31 December 2020). The pore pressure at the well X6 location is about 15.1 MPa at t1 and increases to about 15.7 MPa at t2, whereas the effective stress at well X6 is about 28.7 MPa, and it decreases to about 28.1 MPa at time steps t1 and t2. There is an increase of 0.6 MPa in pore pressure and a decrease of 0.6 MPa in effective stress at the top layer of the reservoir around well X6 from t1 to t2 (Figure 12).

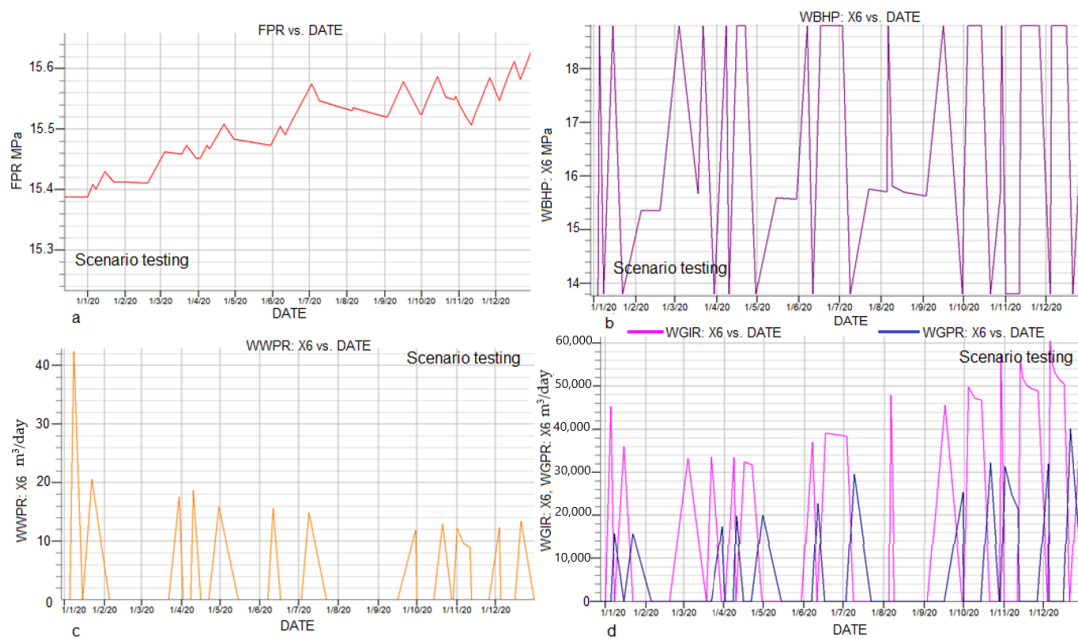


**Figure 11.** The fluctuation of electricity produced in German from renewable sources in 2017 is modelled into a future scenario testing case without limited water cut-off. The excess of energy can be stored in UGS reservoirs and can be used when needed. This schedule is helpful to understand which month of the year's energy can be stored as gas in UGS and in which month of the year this energy can be utilized when shortages occur: (a) field pressure (FPR) profile for these cycles; (b) well bottom hole pressure (WBHP) of well X6; (c) well water production rate (WWPR) for well X6; and (d) injection (WGIR) and production (WGPR) gas rates for well X6.

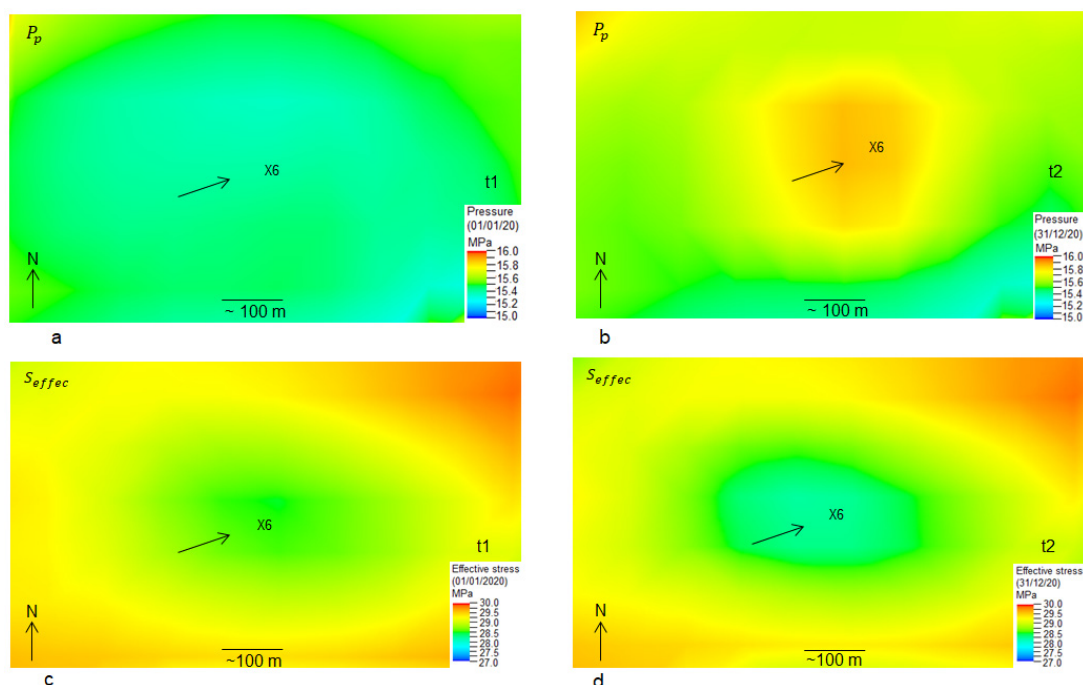


**Figure 12.** Pore pressure ( $P_p$ ) and effective stress ( $S_{effec}$ ) changes from t1 (1 January 2020) to t2 (31 December 2020) in short-term case with one well (X6) without a water cut-off rate of  $5 \text{ m}^3/\text{day}$  with a random schedule. The arrows show the location of the maximum observed fluctuation in  $P_p$  and  $S_{effec}$  from t1 to t2. The color scale is in MPa. (a) is pore pressure at time t1; (b) is pore pressure at time t2; (c) is effective stress at time t1; (d) is effective stress at time t2.

The summary of all the results is compiled in Table 2 to have better understanding of pore pressure and effective stress changes of all future testing cases with time (t1 to t2).

**Table 2.** Summary of results for all future test scenarios. The sign + in the pore pressure changes indicates a positive change or an increase in pore pressure from time step t1 to t2, while the sign— in the changes in effective stresses denotes a decrease in magnitudes of effective stresses for time step t1 to t2. These two quantities are inversely proportional to each other and are expressed in MPa and KPa for a better understanding of the changes.

Modelling Scenarios	Subdivisions	Results	
		Pore pressure changes $\Delta P_p$	Effective stress changes $\Delta S_{effec}$
Short-term (weekly) cases	Case A With three wells (two vertical wells, one horizontal well)	+0.3 MPa +300 KPa	−0.3 MPa −300 KPa
	Case B With three wells (two vertical wells, one horizontal well)	+0.4 MPa +400 KPa	−0.4 MPa −400 KPa
Real-world cases	Case C With one well	+0.6 MPa +600 KPa	−0.6 MPa −600 KPa
	Case D With one well	+0.6 MPa +600 KPa	−0.6 MPa −600 KPa

## 5. Thermal Analysis

The same dynamic model has been used for thermal analyses. Since long-term injection would impact the thermal changes in the reservoir significantly, a long-term seasonal case is used to analyse the temperature changes within the reservoir if a foreign gas is injected into it. Therefore, six months of gas injection and six months of gas withdrawal are considered in this modelling case. The initial reservoir temperature is  $\sim 45^\circ\text{C}$ , and the foreign gas temperature is  $25^\circ\text{C}$ . Two cycles have been considered to analyse the temperature changes during these injection/production operations. Gas is injected into the reservoir for the first half year and produced in the second half of the year. Two wells, X2 and X6, are considered to analyse the temperature changes around the well bore vicinity. The bottom hole pressure (WBHP) for both wells is set to an upper limit of 18.8 MPa and a lower limit of 13.8 MPa in case of the injection and production phases, respectively. These pressure limits are set in place to avoid fault reactivation or fracture-inducing phenomena during the injection phase, as well as to avoid sand production or contraction of the reservoir during the production phase. The WGIR and WGPR are set to  $100,000\text{ m}^3/\text{day}$  for both wells.

Thermal stresses are the stresses that occur due to the change in temperature in the system, i.e., original temperature minus final temperature. If foreign gas is injected into the underground gas reservoir, the temperature in the reservoir changes, which causes thermal-related stress changes in the reservoir. The relationship of temperature changes and thermal stress is expressed by the following equation [34]:

$$S_t = E * \alpha_t (T_f - T_0) = E * \alpha_t (\Delta T), \quad (11)$$

In the above equation,  $S_t$  is thermal stress,  $E$  is the Young's modulus,  $\alpha_t$  is the thermal coefficient,  $T_f$  is the final temperature of the reservoir,  $T_0$  is the original temperature of the reservoir, and  $\Delta T$  is the temperature difference in the reservoir. Less  $\Delta T$  causes less thermal stress in the reservoir and vice versa.

The following section describes the results, i.e., temperature changes with injection of colder foreign gas ( $25^\circ\text{C}$ ) into the reservoir (i.e., about  $45^\circ\text{C}$ ) through space and time with seasonal cyclic injection/production phases. The top view of the reservoir surface is

shown in the figure at different time steps (Figure 13). Two injection/production cycles with four-time steps have been selected to show thermal changes in the reservoir with injection and production phases. Time step t1 (1 January 2020) is the pre-operational history temperature of the reservoir at wells X2 and X6 (Figure 13a). Time step t2 (1 July 2020) represents the end of the injection time of colder foreign gas (25 °C), which is injected for the first half of 2020 (Figure 13b). Time step t3 (1 January 2021) is the end of the production period of the cycle (Figure 13c), and t4 (1 July 2021) is again the end of injection phase of the second cycle (Figure 13d).

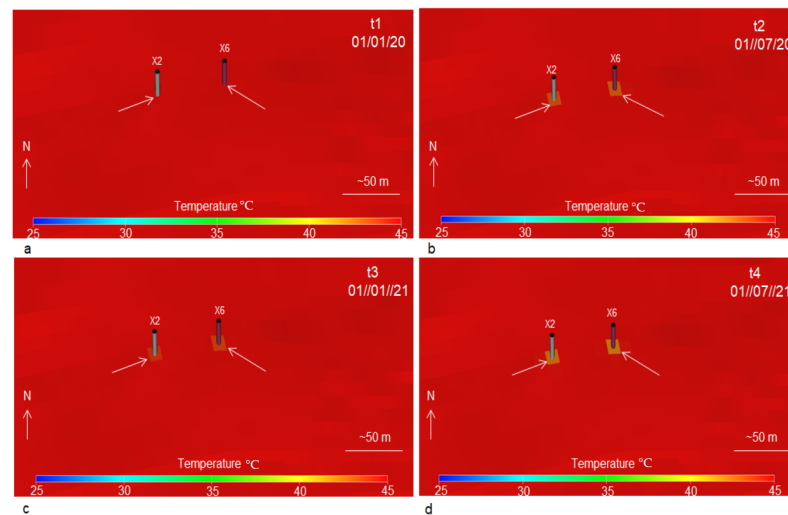


**Figure 13.** Temperature changes around wells X2 and X6 by injecting colder foreign gas at different time steps (t1, t2, t3, and t4). Time steps t1, t2, t3, and t4 correspond to 1 January 2020, 1 July 2020, 1 January 2021, and 1 July 2021, respectively. The arrows show the exact location of significant temperature differences during injection/production phases. The colour scale is in °C, whereas the arrows with N indicate a northward direction. (a) is temperature at time t1; (b) is temperature at time t2; (c) is temperature at time t3; (d) is temperature at time t4.

The reservoir temperature is 45 °C at time step t1, which is the pre-operational temperature. The temperature decreases to about 43 °C at well X6 and 42.5 °C at well X2 at time step t2 after constant injection of colder gas (25 °C), with a well gas injection rate (WGIR) of 100,000 m<sup>3</sup>/day for six months. The temperature increases to about 43.5 °C and ~43 °C at wells X6 and X2, respectively, at time step t3. There is only about a 0.5 °C increase in temperature from t2 to t3. Temperatures at well X6 and X2 decrease to about 41.5 °C and 42 °C, respectively, again in the second cycle of injection at t4. Thermal changes are minor and occur only at the vicinity and around the well locations. The thermal effects on the stress are not significant in the reservoir even after injection of 100,000 m<sup>3</sup>/day of colder gas for about a half year. This outcome shows that the thermal changes in the short-term cases are negligible for analysing the geomechanical stresses on the reservoir in storage operations.

## 6. Potential Fault Reactivation Analyses

### 6.1. Model Setup

Fault reactivation is the possibility of failure in geomechanical assessment of the reservoir, which can risk operational safety, cause micro seismicity within and around reservoirs, and provide a leakage path for gas to escape. Fault reactivation occurs when the shear stress acting on the fault planes exceeds the shear strength of the fault. The

Mohr–Coulomb failure criterion relationship of pore pressure and the principal stresses of this case study reservoir (lies in normal stress regime) are expressed by this equation [35]:

$$P_p = \frac{1}{\alpha} \left[ \frac{1}{2}(S_v + S_{hmin}) + \frac{1}{2}(S_v - S_{hmin}) \cos 2\theta - \frac{1}{2}(S_v - S_{hmin}) \frac{\sin 2\theta}{\mu} \right], \quad (12)$$

where  $\alpha$  is the Biot coefficient (assumed 1),  $S_v$  is the vertical and maximum principal stress,  $S_{hmin}$  is the minimum horizontal stress,  $\theta$  is the angle between the dip line of the fault and the  $S_{hmin}$  direction,  $P_p$  is the critical pore pressure, and  $\mu$  is the coefficient of friction.

These analyses include the calculation of the critical pore pressure with the aim of observing possible differences in pore pressure required for fault reactivation. The pore pressure derived from the history matching scenario is multiplied by a fixed factor controlled by gas rates until fault reactivation occurs. The upper limit of the BHP is removed to obtain a higher pore pressure. The factors used for this operation are 1.15, 1.25, and 1.5 (Figure 14). It is then possible to evaluate pressure changes in the reservoir required to reactivate the fault, as well as the safe storage capacity of the reservoir.

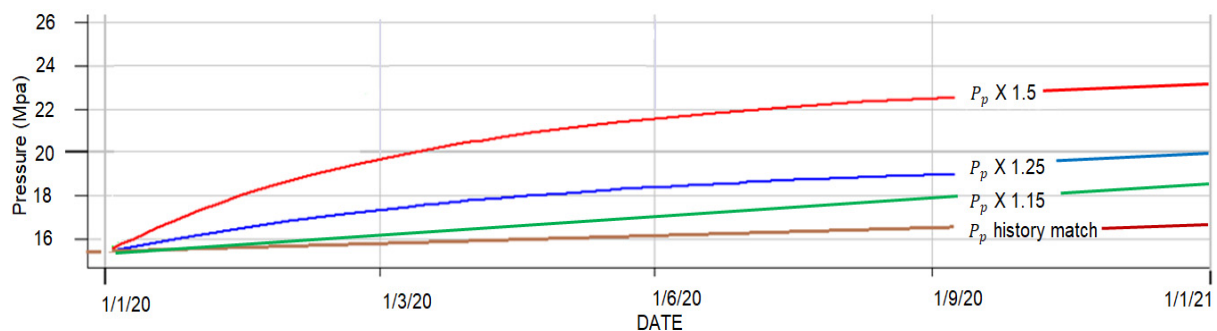


**Figure 14.** Pressure profiles for the history matching scenario and scenarios multiplied by fixed factors ( $P_p$ ,  $P_p \times 1.15$ ,  $P_p \times 1.25$ , and  $P_p \times 1.5$ ) controlled by gas injection rates until fault reactivation occurs.

Figure 14 shows different pressure profiles based on distinct gas injection scenarios. The  $P_p$  (history match pressure) curve exhibits a maximum value of ~16.2 MPa with gas injected at a rate of 100,000 m<sup>3</sup>/day for one year, whereas to reach a pressure value 1.15 times the actual history match pressure case, 175,000 m<sup>3</sup>/day of gas are injected for 1 year. The pressure increased up to 18.6 MPa. In case  $P_p \times 1.25$ , 240,000 m<sup>3</sup>/day is injected to reach a pressure of about 20.25 MPa. Similarly, in case of  $P_p \times 1.5$ , a gas volume of 560,000 m<sup>3</sup>/day is injected (for one year), which increases the pressure up to 24.3 MPa.

## 6.2. Results

The results of this section are based on the model setup explained in the above section. The methodology follows the different cases in which the initial reservoir pore pressure is multiplied by a factor of 1, 1.15, 1.25, and 1.5, corresponding to pore pressure values of ~16.2 MPa, ~18.6 MPa, ~20.25 MPa and ~24.3 MPa, respectively. The results display the oblique view of the topmost layer of the reservoir (Figure 15). The Mohr circles correspond to the well X6 location near the main fault (Figure 15). Two time steps have been considered for all the cases: t1 (1 January 2020) is the starting time step, and t2 (1 January 2021) is the end time step of the schedule year.

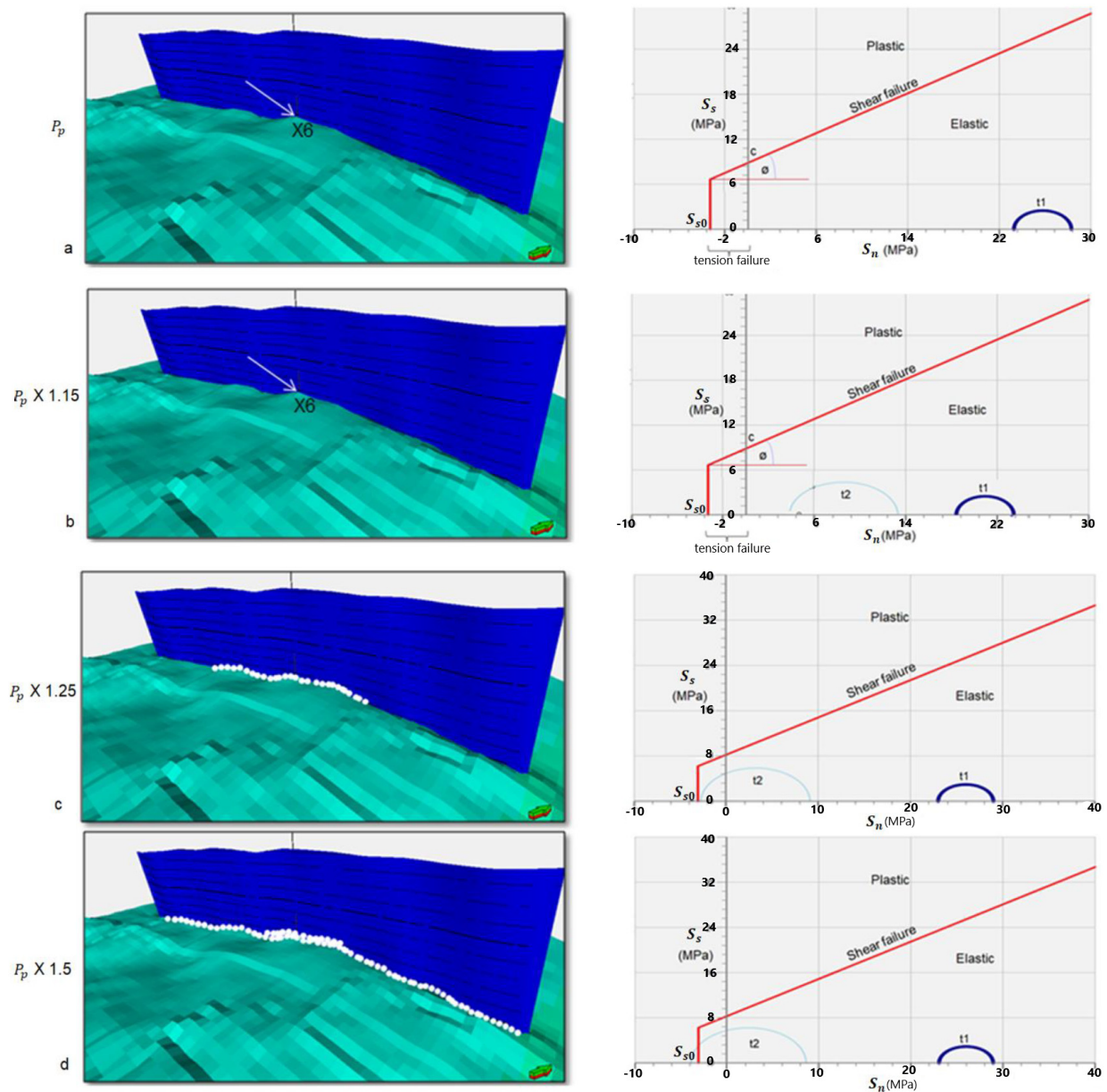


**Figure 15.** The computation of fault reactivation for initial pore pressure multiplied by a factor of 1 (a), 1.15 (b), 1.25 (c), and 1.5 (d) is shown on the left side. White boxes show the cells with stress states exceeding the failure criterion (arrows show northward direction). On the right side of the figure are the shear stress  $S_s$  vs. normal stress  $S_n$  diagrams, showing the Mohr–Coulomb failure criterion at the well X6 location (which is nearest the main fault of the reservoir). Time steps t1 and t2 correspond to the starting (1 January 2020) and final (1 January 2021) time steps of the tested cases, respectively. The increase in pore pressure leads to a decrease in effective stresses, causing the corresponding Mohr circle to shift to the left. If the failure line is finally touched, plastic straining and—in case of a fault zone—fault reactivation occur.

Fault reactivation is observed already at  $P_p \times 1.25$  (~20.25 MPa) (Figure 15b), at which the corresponding Mohr circle has just touched the tensile failure line. The amount of failure in the cells becomes more prominent as pore pressure increases to greater than the pore pressure factor of 1.25 (i.e.,  $P_p \times 1.5$ ), and it causes the corresponding Mohr circles to move further left (Figure 15c,d). The increase in pore pressure causes decreases in effective stress, causing the Mohr circles to move to the tensile failure line. Thereafter, the material enters the plastic regime; therefore, in case of failure, fault reactivation occurs.

### 6.3. Safe Injection Rate for Safe Storage Capacity

The pore pressures for fault reactivation for the different scenarios calculated in the numerical modelling analysis provide an estimate of the pressure at different injection rates. The injection rate (in terms of volume rate) to achieve a perfect history match (16.2 MPa) is about 100,000 m<sup>3</sup>/day, and fault reactivation is already observed at  $P_p$  times 1.25, i.e., about 20.25 MPa at an injection rate of 240,000 m<sup>3</sup>/day. With the determination of the critical pore pressure, it is also possible to derive an upper limit for the injection rate to be selected for injection processes. By considering the highest safety margin, the injection rate between 100,000 m<sup>3</sup>/day and 150,000 m<sup>3</sup>/day would be the considered safe injection rate for safe storage for the case study reservoir. A gas injection rate greater than this threshold value can have a significant impact on the risk management and operational setup of underground gas storage.

### 6.4. Storage Capacity of Power-to-Gas and Gas-to-Power

Regarding the storage capacity of power-to-gas technologies, the case study reservoir can store 881,600 kWh/d up to maximum of 1,322,400 kWh/d of power from renewable or other resources with respect to the conversion of a natural gas volume of 100,000 m<sup>3</sup>/day to a maximum of 150,000 m<sup>3</sup>/day, respectively. Power-to-gas and gas-to-power convertible units are summarized in Table 3.

**Table 3.** Power-to-gas and gas-to-power convertible units.

m <sup>3</sup> Natural Gas	kWh Power
1	8.816
0.113	1

## 7. Discussions

### 7.1. Hydraulic Model

The results of the hydraulic model show variations in gas saturation at different phases during short-term injection-production cycles. Figure 16 shows that the injection-production cycle increases the gas saturation during the later cycles, as more gas is produced with increasing cycles until convergence is reached. This outcome indicates the adoption of high-speed multicycle injection-production in UGS with time. This characteristic of UGS indicates the increase in gas-containing pore space with time and explains encroachment of gas flow continuously into the ground water zone for production in the pore throat development area, as the injection-production cycle increases. Meanwhile, under the wetting function, the water film is concentrated in the small pore space compared to the larger pore space; the storage space occupied by the formation of water and dead gas zones is released by the gas execution. Further analysis of the data shows notable findings on the correlation between the time and the amplitude of the gas saturation increase, as shown in Figure 16.

During injection and production cycles, gas saturation increases from ~35% to ~50% from the first cycle to the sixth cycle. Therefore, it appears that, during multi-cycle injection and production in the pre-UGS gas zone, the pore gas storage space in reservoirs with low permeability generally increases sharply, as evident from the correlation between low permeability and high initial water saturation (according to [6]). Moreover, the higher the relative quantity of liquid phase that is continuously transported and dried during high velocity development, the greater the increase in gas saturation.

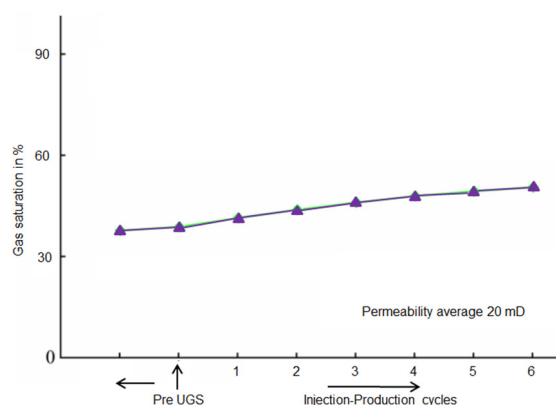


**Figure 16.** Gas saturation (%) during injection-production cycles.

The gas injection production capacity tends to improve in the UGS gas zone when gas production is increased during the injection production cycle. Further investigation of the UGS gas zone shows that the degree of gas production also increases with the injection-production cycle, but the degree of gas production varies according to the different physical properties and connectivity of the pore spaces [6]. Strong seepage is observed in reservoirs with high permeability, and the gas production and degree of gas recovery are also high under the same injection-production conditions [6].

The gas saturation first decreases in the pre UGS phase and then increases significantly during multi-cycle injection and production, showing the decrease in gas saturation and gas storage space when the gas-drive water zone (gas-water zone, where gas saturation is more dominant) is converted into gas storage. Due to the intrusion of lateral and bottom water, part of the gas storage space is occupied by water during the slow exploitation phase, and a capillary trap for the gas-containing space is also created. Further data show that higher permeability causes water to penetrate, leading to an even greater reduction in gas saturation. During the multi-cycle injection and production phase in UGS, there is no water encroachment, or the part where water encroachment occurs is displaced in the initial gas injection phase of gas storage into the gas-drive water zone. In contrast, under the influence of high velocity injection and production cycle extraction, residual water is produced that is like that in the gas zone before UGS [6]. The experimental analysis shows that the gas-drive water zone is the main expansion zone of the UGS, as the storage space and storage capacity are greatly increased in this gas-drive water zone [6].

The variation of gas saturation in the gas-drive water zone shows the same trends compared to both the trend in the single core experiment and the trends of average gas saturation in the parallel multicore experiment. However, in the multicore parallel experiment, the reduction in gas saturation caused by water encroachment is relatively small [6]. The distinctive feature of reservoir heterogeneity, a formation with high permeability, has a great impact on the water body as it promotes water intrusion, while formations with medium and low permeability are less affected by water intrusion. During high velocity injection and production, the gas preferentially percolates into the high permeability formation, resulting in gas saturation recovery in the high permeability reservoir.

The gas permeability of the reservoir may also decrease due to clay minerals in the reservoir, which may expand when they encounter water, thereby occupying the pore space. For this reason, gas production and gas content are relatively low in the first injection and production cycle. Meanwhile, the gas recovery level and gas production level are low due to lower vertical permeability [6]. Furthermore, gas production and injection increase with increasing permeability.

The transition of the reservoir characteristic of the gas-water transition may indicate that water intrusion is caused not only by exploitation of the gas field but also by the gas storage cycle in the operational phase. In general, the gas saturation decreases both in operational zones of the reservoir and in the gas-water zone. However, the effects of

physical properties and heterogeneity, wettability, and capillary pressure of the reservoir make the production mechanism of multicycle injection complex. The relationship between gas and water in the gas-water transition zone tends to be rational, and the gas saturation tends to plateau during multicycle injection production [6]. Alternatively, residual gas and trapped gas are effectively reduced due to the back-and-forth movement of gas and water through the gas-containing spaces, but the changes in gas saturation are small throughout the reservoirs. Conversely, in high-speed injection and production, water is still continuously transported into the pore throat for production, but in gas storage, the main discharge concerns water in the large pore throat because it is difficult to displace water in the micropores. For this reason, gas saturation tends to plateau in the gas-water transition zone. Due to the reduction in water intrusion energy, gas saturation increases slightly in the subsequent phases of injection and production operations.

These results show that low gas saturation and poor recovery are observed in the gas-water transition zone of UGS and that effective exploitation of the gas-water transition zone is affected by reservoir heterogeneity [6]. Therefore, the effective utilization of the gas-containing pore space under the high-speed injection and production conditions of gas storage is significantly different from the utilization of the gas reservoir. For that reason, the optimal design of UGS capacity and calculation of gas storage parameters should be founded on the effective utilization of the gas-containing pore space, as well as on the effective pore space of the reservoir structure in different zones [6].

### 7.2. THM Coupled Modelling

The geomechanical approach presented in this paper allows for characterization, from a geomechanical point of view, of the target reservoir in a very understandable way. The coupled simulation of one-way flow and geomechanics (VISAGE™) focuses on understanding the variation in effective stresses due to pressure changes associated with gas injection into the subsurface reservoir. In other words, the focus is on the pore pressure changes during operation. The VISAGE™ model is created directly from the geological model and can therefore be considered more accurate in terms of geometry compared to another finite element model, such as an ANSYS™ model. The material properties in the VISAGE™ model are scaled up from borehole logs, and their population contains information about the original vertical and horizontal variations. The VISAGE™ simulator treats faults as 3D cells with different material parameters in relation to the surrounding rock. The output of the VISAGE™ model is continuous through space, and the presence of faults can be detected by an abrupt change in depth at the point of displacement, even if the horizon is technically not present at that point. Therefore, VISAGE™ is used for ECLIPSE™-VISAGE™ coupling to build a coupled THM model to achieve the desired geomechanical results.

THM coupled modelling involves coupling of static geomechanical model with dynamic fluid (hydraulic) modelling. The geomechanical stresses of the reservoir change in space and time when coupled with pore pressure, either from reservoir history or from future testing scenarios. In general, these dynamic models are based on the concept of effective stress to characterize the effects of pore pressure changes on reservoir and caprock integrity, as well as fault stability. Simplified geomechanical models rely mainly on the concept of effective stress to distinguish the effects of pore fluid changes on reservoir integrity and fault stability. Terzaghi [36] proposed this effective stress concept for soil systems. The result of the increase in pore fluid pressure is equal to the decreased effective stress on the rock mass, and conversely, this concept implies that the effective stress experienced by the rock framework is due to the changes in fluid pressure, with the absolute magnitudes of the principal in situ stresses themselves remaining unaltered.

From a classical point of view from Terzaghi [36], changes in vertical stress can be predicted as the effective vertical stress increases and decreases during withdrawal and injection, while the reservoir stress path effect can clearly distinguish the changes in the effective minimum horizontal stresses. As a result of the increased fluid pressure, the Mohr

circle drifts to the left, in turn reducing the diameter of the circle, implying that the fault is under a lower differential stress. The theoretical viewpoint consolidates only the concept of effective stress, and the assumption can be made that the stress path during compression is parallel to the failure envelope rather than towards it [2]. A steeper stress path during the injection process is the result of a small Poisson's ratio, a large Biot coefficient, a large shear modulus, and a shallower reservoir, further causing drift away from the failure envelope.

At the case study reservoir, reactivation of the fault with increasing fluid pressure would not be possible if the stress path could be assumed to be exactly linear to higher fluid pressures. The magnitude of the stress path in the reservoir is an absolute criterion to ensure that the faults are not tapered by pressurization or depressurization. Furthermore, this linear extrapolation of the stress path is obviously only suitable for moderate fluid pressure levels. During pressurization of the system, there are some points at which the horizontal stress becomes the maximum principal stress instead of the vertical stress. This outcome shows that, in the absence of stress path effects, the stress path changes and moves towards the failure criterion.

One of the main aspects of the THM modelling results is the deformation within and outside of the reservoir formation because of injection and withdrawal of fluid/gas in reservoirs. Pressurization and depressurization cause deformations in both the reservoir and the overburden, which are part of the effective results of geomechanical modelling. During overpressure or underpressure, the elastic or non-elastic expansion or contraction of the rock mass causes such deformations. The reactivation of faults and the integrity of the rock may be affected by deformations within the reservoir. In addition, deformations associated with reservoir depletion can also pose a serious problem in terms of casing collapse and can become a major obstacle to subsequent drilling [37].

The main risks related to pressurization and depressurization of a field during injection and withdrawal periods, respectively, are fault reactivation and associated permeable leakages. During gas injection and production phases, reactivation of the fault and associated permeable pathways is one of the main risks associated with pressurization and depressurization. The classical fault model would predict that, as the fault approaches shear reactivation, there will be an increase in fluid pressure that would reduce the effective normal stress on the fault. However, the stability of the fault is significantly affected by the progression of reservoir stresses through the effects on horizontal stress magnitudes. As discussed in the above section, the simulation results of the THM model predict decreases in effective stresses but increases in pore pressure in various short-term storage cases. If this difference in effective stresses and consequently in pore pressures is very small, no significant stress perturbations would occur. However, if this difference is large, i.e., if the pore pressure in the reservoir is large, then there is a high probability of fault reactivation with increasing pore pressure, as described in the above regarding the various fault reactivation cases. Fault reactivation occurs in the reservoir already at 1.25 times the initial pore pressure of the reservoir, indicating that the Mohr circle reaches the failure line at this pressure.

Distinguishing deformations above and at the surface of the reservoir is also important for surface monitoring and for potential reactivation of faults in the reservoir section. These deformations (either elastic or sometimes plastic) occur due to contraction and expansion of the rock mass during over-pressuring and under-pressuring phases. Over- and under-pressuring of reservoirs are directly related to large amounts of gas injection and production rates, respectively. For this reason, the upper (18.8 MPa) and lower (13.8 MPa) limits of bottom hole pressure (BHP) are considered, which do not allow the pressure to rise or drop below the designated pressure limits. The deformation caused by this over-pressuring and under-pressuring of reservoirs could initiate fault reactivation and may affect caprock integrity. The significant drop in reservoir pressure due to rapid depletion may damage the casing and induce drilling complications for newly planned wells in the reservoir [37].

This study does not include a sensitivity analysis to determine the stress field or displacement of the ground surface when elastic properties vary. Due to the poor correlation

between the mechanical properties of the rock and the porosity in the individual wells, there can be considerable variation in the construction of the static geomechanical model, which can affect the distribution of the mechanical properties, rather than the magnitudes. In contrast, the successive calibration of the sonic logs and the mechanical tests themselves appear to have close correlations, demonstrating their accuracy. However, it is possible that the actual values for Poisson's ratio and Young's modulus may differ slightly from those used in the modelling. There are several studies that have already been performed on these parameter studies and the effects of parameter variation on geomechanical stresses and ground surface displacement [38]. Chen (2012) modelled the pressurization of a reservoir at 600 m of depth by 1 MPa using Young's modulus and Poisson's ratio values close to our case study reservoir. This modelling study suggests reducing the stiffness of the reservoir; i.e., reducing the value of Young's modulus from 5 GPa to 3 GPa, the vertical displacement increases from 0.08 to 0.12 mm [38]. Similarly, a reduction in the Poisson ratio from 0.3 to 0.2 results in an increase in the ground surface displacement from 0.11 to 0.13 mm [38]. It should be borne in mind that the sensitivity of these parameters is highly dependent on several different factors, including the depth and size of the reservoir, the stress field, and the properties attributed to the surrounding formations [38]. However, the work presented by Chen gives a rough idea of the types of variations that might be expected from such modelling.

## 8. Conclusions

THM modelling provides important results for short-term gas storage, e.g., conversion of the former gas field to a storage site with short-term (weekly) injection-production schedules. There have been three cases tested for future scenarios with short-term operations. German surplus energy data from renewable energy sources (such as wind and solar energy) from 2017 have also been incorporated into these future testing cases to implement PtG technology on former gas reservoirs to meet Germany's future energy demand. The operating volumes in these cases are controlled by the upper (18.8 MPa) and lower limits (13.8 MPa) of well bottom hole pressure (WBHP). The results of the coupled THM modelling of these cases show that the maximum difference in pore pressure and subsequently effective stress is observed to be 0.6 MPa among all tested cases.

Fault reactivation analyses are performed on the THM models, which evaluate various gas injection scenarios without any upper limit of WBHP. The quantified stresses are then examined against Mohr–Coulomb failure criterion to estimate fault stability. This goal is achieved by including faults with specific properties in the 3D geomechanical model. The stress state of the 3D cells with fault properties exceeding the shear failure line is observed against different gas injection volumes. Fault reactivation occurred at the gas injection rate of 240,000 m<sup>3</sup>/day, yielding a value of critical pore pressure. This critical pore pressure was observed to be 1.25 times the original pore pressure, which is equivalent to the WBHP value of 20.25 MPa. With the determination of pore pressure, it is also possible to estimate an upper limit of the gas injection rate for safe storage operation, which in this case study is observed to be in the range between 100,000 and 150,000 m<sup>3</sup>/day.

In this study, the critical pore pressure is calculated at the well location, whereas the reference location for further studies can be anywhere in the reservoir, and the high permeability of the reservoir can reduce possible differences in the reference sites. Analysis of the case study numerical modelling results shows that a 4-MPa increase in pore pressure would be sufficient to trigger fault failure.

Thermal stresses depend merely upon the thermal-dynamic processes in the system. Therefore, one case (seasonal) has been tested for thermal stress analysis using the same THM model. The original reservoir temperature is 45 °C, and the injected gas temperature is set at 25 °C. The thermal changes are small (0.5 °C) and occur only near and around the wellbore. The thermal effects on stress are not significant in the reservoir, even after injecting 100,000 m<sup>3</sup>/day of colder gas for about half a year. This outcome suggests that the thermal changes in the short-term cases are negligible to be considered in the analysis.

of geomechanical stresses in the reservoir during storage operations. This finding is due to the low operating volumes and short time cycles for injection production (weekly schedule) in short-term cases.

In terms of storage capacity of PtG technologies, the case study storage can store up to maximum of 1,322,400 kWh/d of electricity from renewable or other resources, converting the maximum gas volume of 150,000 m<sup>3</sup>/day. This amount of energy storage can at least contribute to Germany becoming a greenhouse gas neutral country (GHGND) in 2050, corresponding to an energy demand of 1600 TWh of electricity.

The entire workflow outlined and tested in this study is not site specific but generally applicable to any gas storage in a porous medium including methane, CO<sub>2</sub>, and hydrogen.

### *Perspectives*

The modelling schemes described in this study provide a thermal-hydraulic-geomechanical assessment consistent with the observational data presently available. This THM modelling study can be used to assess borehole stability, which can be achieved by analysing the hydraulic and mechanical limits of the borehole walls. Another application of the model can be a fully coupled model, in which geomechanical and hydraulic models are coupled in such a way that both can receive and process the required parameters simultaneously (explained in the last paragraph). This modelling study can also serve as a benchmark for the use of UGS as a seasonal battery for PtG technologies. In this way, the excess energy can be stored as gas in the UGS and later converted back into electricity when needed.

The rock properties of the reservoir have an important influence on the estimated amount of subsidence. For future modelling, it would be useful to conduct detailed rock mechanics experiments with representative samples from the deposits in the region. It is important to have as much reliable data as possible on vertical elevation changes in the region to test different hypotheses related to subsidence. Such data could come from repeated surveys of existing first-order contour lines, GPS, or InSAR observations. In addition, sensitivity analyses or parameter studies to determine the stress field or displacement of the ground surface as elastic properties vary would be useful to understand the reservoir behaviour in response to changes in, for example, Young's modulus or Poisson's ratio.

THM modelling in this study uses a one-way coupling simulation approach. The coupling between dynamic fluid flow and geomechanical simulation can be improved by adopting two-way or even fully coupled simulations. Such a simulation means that not only the pore pressure is passed from the fluid flow model to the geomechanical model, but also properties from the geomechanical model, such as porosity, permeability, and rock compressibility, are passed back to the fluid flow model to obtain continuously updated accurate modelling results. Two-way and fully coupled simulation approaches would also be useful to analyse ageing effects in reservoirs due to long- and short-term storage operations.

**Author Contributions:** Conceptualization, M.Z.-U.-A. and A.H.; methodology, M.Z.-U.-A.; software, M.Z.-U.-A.; validation, M.Z.-U.-A. and A.H.; formal analysis, M.Z.-U.-A.; investigation, M.Z.-U.-A.; resources, M.Z.-U.-A.; data curation, M.Z.-U.-A.; writing—original draft preparation, M.Z.-U.-A.; writing—review and editing, A.H.; visualization, M.Z.-U.-A.; supervision, A.H.; project administration, A.H.; funding acquisition, A.H. All authors have read and agreed to the published version of the manuscript.

**Funding:** This research was funded by BMBF (Federal Ministry of Education and Research), grant number 03G0869.

**Data Availability Statement:** Data available in a publicly accessible repository. The data presented in this study are openly available in [TUPrints, Darmstadt] at [DOI: 10.26083/tuprints-00022537, CC-BY-SA 4.0 International].

**Acknowledgments:** The authors thank Uniper SE for providing data for this research. We acknowledge the German Federal Ministry of Education and Research (BMBF) for providing financial support for the SUBI research project. In addition, we acknowledge support from the Deutsche Forschungsgemeinschaft (DFG, German Research Foundation) and the Open Access Publishing Fund of the Technical University of Darmstadt.

**Conflicts of Interest:** The authors declare no conflict of interest.

## References

1. Teatin, P.; Castelletto, N.; Ferronato, M.; Gambolati, G.; Janna, C.; Cairo, E.; Marzorati, D.; Colombo, D.; Ferretti, A.; Bagliani, A.; et al. Geomechanical response to seasonal gas storage in depleted reservoirs: A case study in the Po River basin, Italy. *J. Geophys. Res. AGU J.* **2011**, *116*, 21. [[CrossRef](#)]
2. Tenthorey, E.; Vidal-Gilbert, S.; Backe, G.; Puspitasari, R.; Pallikathakathil, Z.; Maney, B.; Dewhurst, D. Modelling the geomechanics of gas reservoir: A case study from the Iona gas field, Australia. *Int. J. Greenh. Gas Control* **2013**, *13*, 138–148. [[CrossRef](#)]
3. Aminian, K.; Brannon, A.; Ameri, S. Gas storage in a depleted gas/condensate reservoir in the appalachian basin. In Proceedings of the SPE Eastern Regional Meeting, Canton, OH, USA, 11–13 October 2006.
4. Juez-Larre, J.; Rimmelts, G.; Breunese, J.; Van Gessel, S.Q.; Leeuwenburgh, O. Using underground gas storage to replace the swing capacity of the giant natural gas field of Groningen in the Netherlands. A reservoir performance feasibility study. *J. Pet. Sci. Eng.* **2016**, *145*, 34–53. [[CrossRef](#)]
5. Industry, D.O.T.A. *Meeting the Energy Challenge: A White Paper on Energy*; Her Majesty's Stationary Off.: Norwich, UK, 2007.
6. Zhang, J.; Fang, F.; Lin, W.; Gao, S. Research on Injection-Production Capability and Seepage Characteristics of Multi-Cycle Operation of Underground Gas Storage in Gas Field—Case Study of the Wen 23 Gas Storage. *Energies* **2020**, *13*, 17. [[CrossRef](#)]
7. Kuncir, M.; Chang, J.; Mansdorfer, J.; Dougherty, E. Analysis and optimal design of gas storage reservoirs. In Proceedings of the SPE Eastern Regional Meeting, Pittsburgh, PA, USA, 6–10 September 2003; pp. 1066–1076.
8. Mazarei, M.; Davarpanah, A.; Ebadati, A.; Mirshekari, B. The feasibility analysis of underground gas storage during an integration of improved condensate recovery processes. *J. Pet. Explor. Prod. Technol.* **2019**, *9*, 397–408. [[CrossRef](#)]
9. Dharmananda, K.; Kingsbury, N.; Singh, H. Underground gas storage: Issues beneath the surface. In Proceedings of the SPE Asia Pacific Oil and Gas Conference and Exhibition, Perth, Australia, 18–20 October 2004; pp. 10–17.
10. Abedin, M.Z.; Henk, A. Building 1D and 3D Mechanical Earth Models for Underground Gas Storage—A Case Study from the Molasse Basin, Southern Germany. *Energies* **2020**, *13*, 21.
11. Khaksar, A.; White, A.; Rahman, K.; Burgdorff Kollarves, R.; Dunmore, S. Geomechanical Evaluation for Short Term Gas Storage in Depleted Reservoirs. In Proceedings of the 46th US Rock Mechanics/Geomechanics Symposium, Chicago, IL, USA, 24–27 June 2012.
12. Bachmann, G.H.; Müller, M.; Weggen, K. Evolution of the Molasse Basin (Germany, Switzerland). *Tectonophysics* **1987**, *137*, 77–92. [[CrossRef](#)]
13. Dake, L.P. *Fundamentals of Reservoir Engineering*; Elsevier Scientific Pub. Co.: Amsterdam, The Netherlands, 1978.
14. Dai, W.J.; Gan, Y.X.; Hanaor, D. Effective Thermal Conductivity of Submicron Powders: A Numerical Study. *Appl. Mech. Mater.* **2015**, *846*, 500–505. [[CrossRef](#)]
15. Settari, A.; Mourits, F. A Coupled Reservoir and Geomechanical Modeling System. *SPE J.* **1998**, *SPE 50939*, 219–226. [[CrossRef](#)]
16. Tortike, W.; Farouq, A.S. Reservoir Simulation Integrated with Geomechanics. *J. Can. Pet. Technol.* **1993**, *5*, 28–37. [[CrossRef](#)]
17. Jalali, M.R.; Dusseault, M.B. Coupling Geomechanics and Transport in Naturally Fractured Reservoirs. *Int. J. Min. Geol. Eng. (IJMGE)* **2012**, *46*, 105–131.
18. Mainguy, M.; Longuemare, P. Coupling Fluid Flow and Rock Mechanics: Formulation of the Partial Coupling between Reservoir and Geomechanical Simulators. *Oil Gas Sci. Technol.* **2002**, *57*, 355–367. [[CrossRef](#)]
19. Perkins, T.K.; Gonzalez, J.A. The Effect of Thermoelastic Stresses on Injection Well Fracturing. *Soc. Pet. Eng.* **1985**, *25*, 78–88. [[CrossRef](#)]
20. Geertsma, J. Problems of Rock Mechanics in Petroleum Production Engineering. *First Congr. Int. Soc. Rock Mech.* **1966**, *1*, 585–594.
21. Skempton, A. The Pore Pressure Coefficients A and B. *Geotechnique* **1954**, *4*, 143–147. [[CrossRef](#)]
22. Geertsma, J. The Effect of Pressure Decline on Volumetric Changes of Porous Rocks. *Trans. AIME* **1957**, *201*, 331–340. [[CrossRef](#)]
23. Van der Knaap, W. Nonlinear Behavior of Elastic Porous Media. *Trans. AIME* **1959**, *216*, 179–187. [[CrossRef](#)]
24. Nur, A.; Byerlee, J. An Exact Effective Stress Law for Elastic Deformation of Rock with Fluid. *J. Geophys. Res.* **1971**, *76*, 6414–6418. [[CrossRef](#)]
25. Ghaboussi, J.; Wilson, E. Flow of Compressible Fluid in Porous Elastic Media. *Int. J. Numer. Methods Eng.* **1973**, *5*, 419–442. [[CrossRef](#)]
26. Rice, J.; Cleary, M. Some Basic Stress-Diffusion Solutions for Fluid Saturated Elastic Porous Media with Compressible Constituents. *Rev. Geophys. Space Phys.* **1976**, *14*, 227–241. [[CrossRef](#)]
27. Huan, X.; Xu, G.; Zhang, Y.; Sun, F.; Xue, S. Study on Thermo-Hydro-Mechanical Coupling and the Stability of a Geothermal Wellbore Structure. *Energies* **2021**, *14*, 649. [[CrossRef](#)]

28. Rutqvist, J.; Wu, Y.; Tsang, C.F.; Bodvarsson, G. A modeling approach for analysis of coupled multiphase fluid flow, heat transfer, and deformation in fractured porous rock. *Int. J. Rock Mech.* **2002**, *39*, 429–442. [[CrossRef](#)]
29. Pang, M.; Xu, G.; Sun, F.; Xue, S.; Wang, Y. Formation Damage and Wellbore Stability of Soft Mudstone Subjected to Thermal–Hydraulic–Mechanical Loading. *J. Eng. Sci. Technol.* **2019**, *12*, 95–102. [[CrossRef](#)]
30. Hu, L.; Winterfeld, P.H.; Fakcharoenphol, P.; Wu, Y.S. A novel fully-coupled flow and geomechanics model in enhanced geothermal reservoirs. *J. Pet. Sci. Eng.* **2013**, *107*, 1–11. [[CrossRef](#)]
31. Tran, D.; Nghiem, L.; Buchanan, L. *Improved Iterative Coupling of Geomechanics with Reservoir Simulation*; Society of Petroleum Engineers: Houston, TX, USA, 2005.
32. Frey, C. Ministerin Hendricks: Wir Haben im Gegenteil Sogar Gigantische Stromüber-Schüsse. 2018. Available online: <https://eike-klima-energie.eu/2018/01/07/ministerin-hendricks-wir-haben-im-gegenteil-sogar-gigantische-stromueberschuesse/?print=pdf> (accessed on 1 June 2020).
33. Burger, B. Fraunhofer ISE Fraunhofer ISE, Freiburg. 2018. Available online: [https://www.ise.fraunhofer.de/content/dam/ise/de/documents/publications/studies/daten-zu-erneuerbaren-energien/Stromerzeugung\\_2017.pdf](https://www.ise.fraunhofer.de/content/dam/ise/de/documents/publications/studies/daten-zu-erneuerbaren-energien/Stromerzeugung_2017.pdf) (accessed on 1 June 2020).
34. Carter, G.F.; Paul, D.E. *Materials Science & Engineering, Materials Park Ohio*; ASM International: Novelty, OH, USA, 1991.
35. Fjaer, E.; Holt, R.M.; Horsrud, P.; Raaen, A.M.; Risnes, R. *Petroleum Related Rock Mechanics*; Elsevier Science: Oxford, UK, 2008; p. 514.
36. Terzaghi, K. *Theoretical Soil Mechanics*; Chapman and Hall Limited: London, UK, 1948.
37. Zoback, M. *Reservoir Geomechanics*; Cambridge University Press: Cambridge, UK, 2007; p. 449.
38. Chen, Z.R. Poroelastic model for induced stresses and deformations in hydrocarbon and geothermal reservoirs. *J. Pet. Sci. Eng.* **2012**, *80*, 41–52. [[CrossRef](#)]

**Disclaimer/Publisher’s Note:** The statements, opinions and data contained in all publications are solely those of the individual author(s) and contributor(s) and not of MDPI and/or the editor(s). MDPI and/or the editor(s) disclaim responsibility for any injury to people or property resulting from any ideas, methods, instructions or products referred to in the content.